Computing at the Moiré Scale

Mitchell Luskin
University of Minnesota

IPAM, UCLA

April 22, 2023

Hofstadter's Butterfly

Harper's Equation

$$2\psi_\ell \cos(2\pi\ell b - \kappa) + \psi_{\ell+1} + \psi_{\ell-1} = E\psi_\ell$$

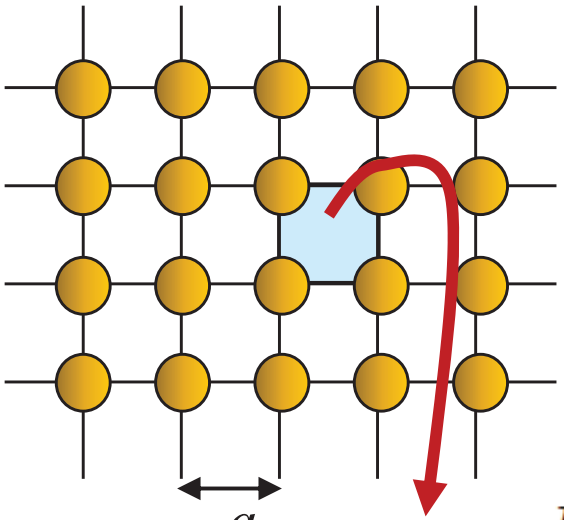

$$b = \frac{Ba^2}{\phi_0} = \frac{\phi}{\phi_0}$$

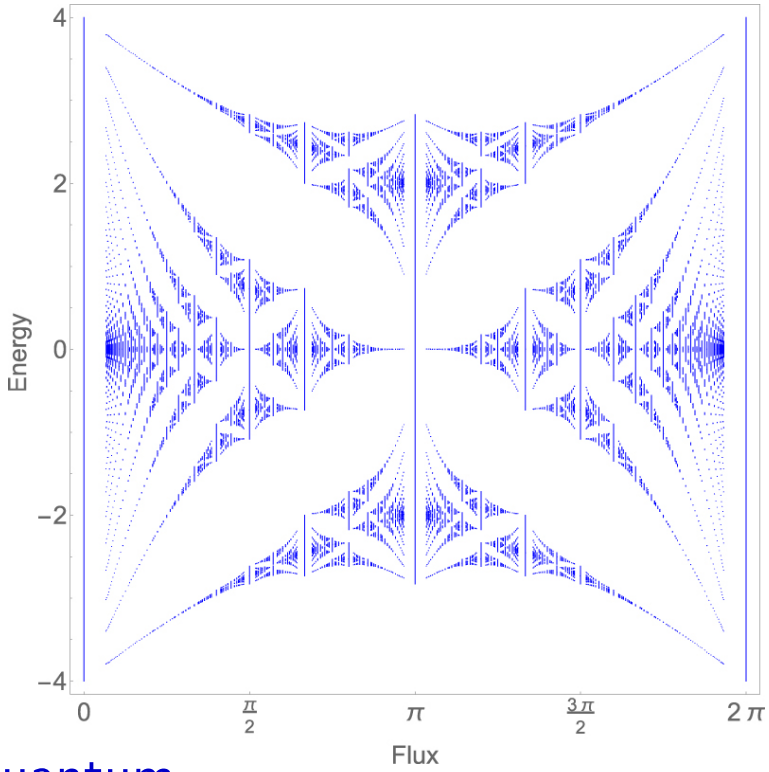

where $\phi_0 = 2\pi\hbar/e$ is the magnetic flux quantum.

"At first glance, the idea seems totally out of the range of possibility, since. . . the rather generous lattice spacing of $a = 2$ Å demands a magnetic field of roughly 10^9 G."

Douglas Hofstadter (1976), "Energy levels and wavefunctions of Bloch electrons in rational and irrational magnetic fields." Physical Review B 14 (6).

The Moiré Superlattice for Twisted Bilayer Graphene

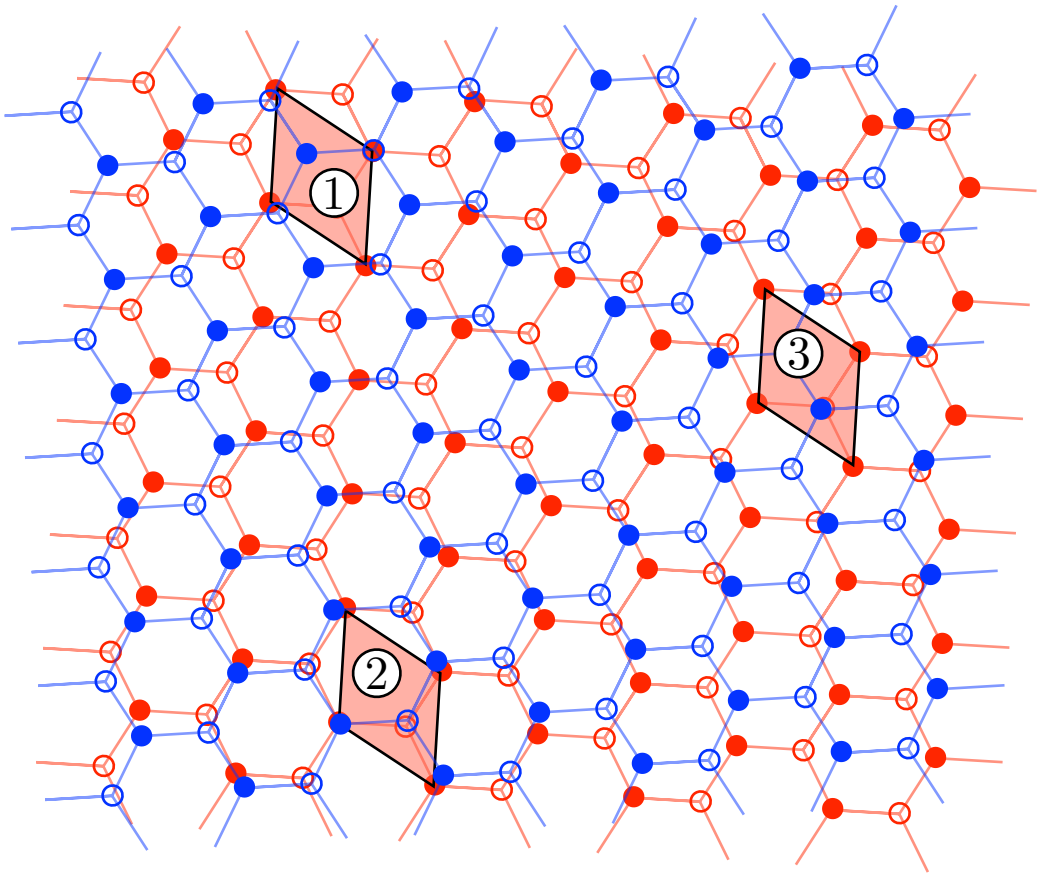

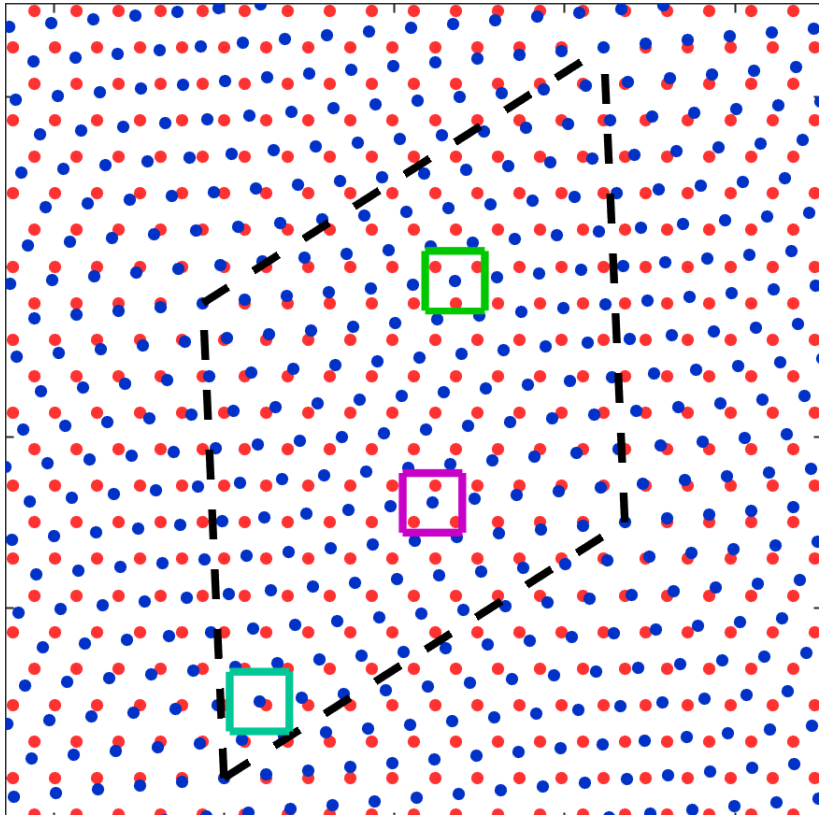

Moire patterns as beating phenomena

Consider oscillations $h_\ell(r) = \sum_{k=1}^{2} e^{ib_{\ell,k}\cdot r}$ of twisted layers ℓ with wave vectors $b_{\ell,k}$.

$$h_M(r) = h_1(r) + h_2(r) = \sum_{k=1}^{2} e^{i\left(\frac{b_{1,k}+b_{2,k}}{2}\right)\cdot r} e^{\pm i\left(\frac{b_{1,k}-b_{2,k}}{2}\right)\cdot r}.$$

Fast **atomistic scale** oscillations with wave vectors $\left(\frac{b_{1,k}+b_{2,k}}{2}\right)$.

Slow **moiré scale** envelope function with moiré wave vectors $\left(\frac{b_{1,k}-b_{2,k}}{2}\right)$.

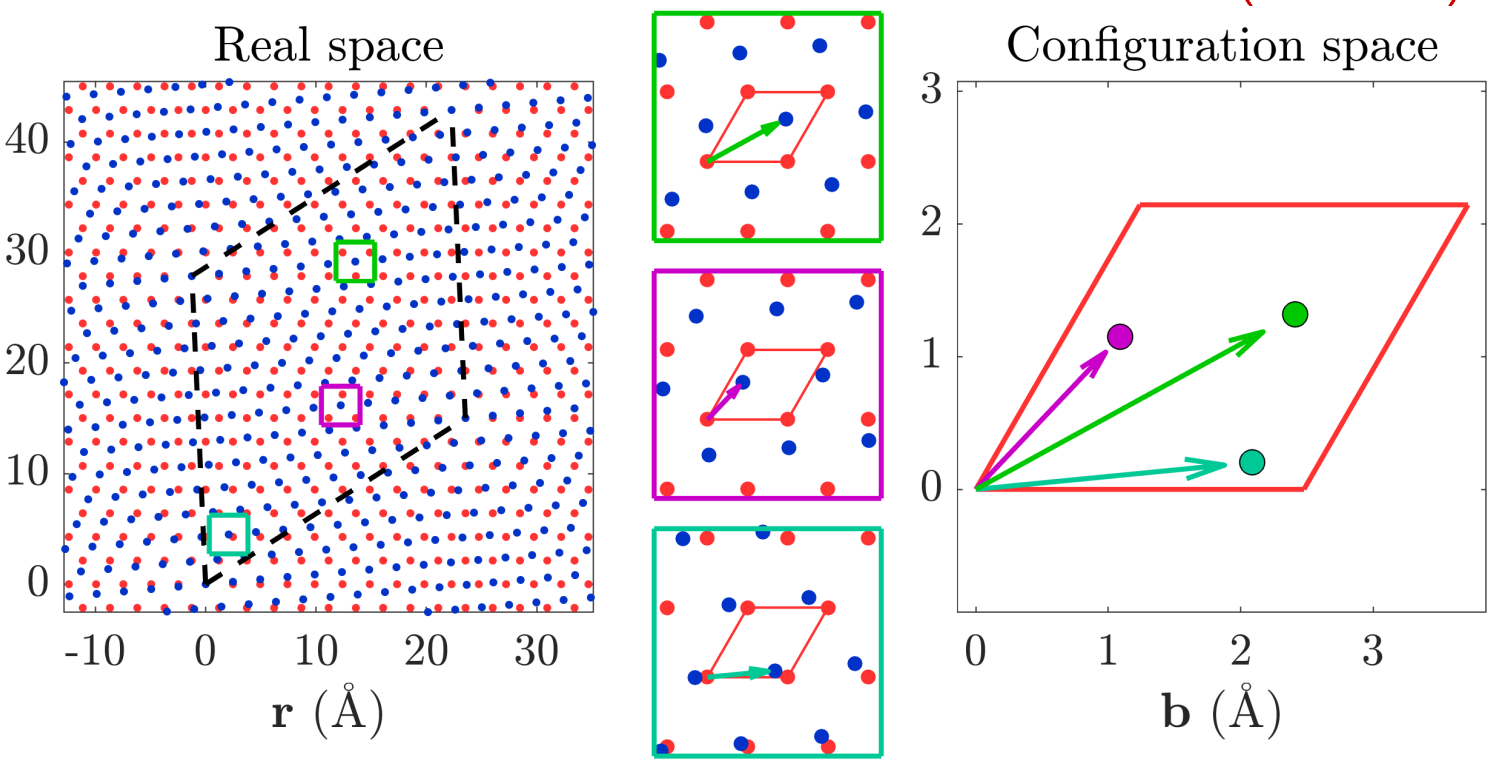

Capturing Hofstadter's Butterfly in Twisted Bilayer Graphene/hBN

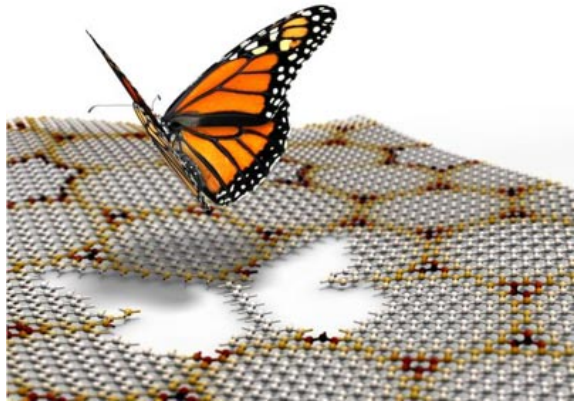

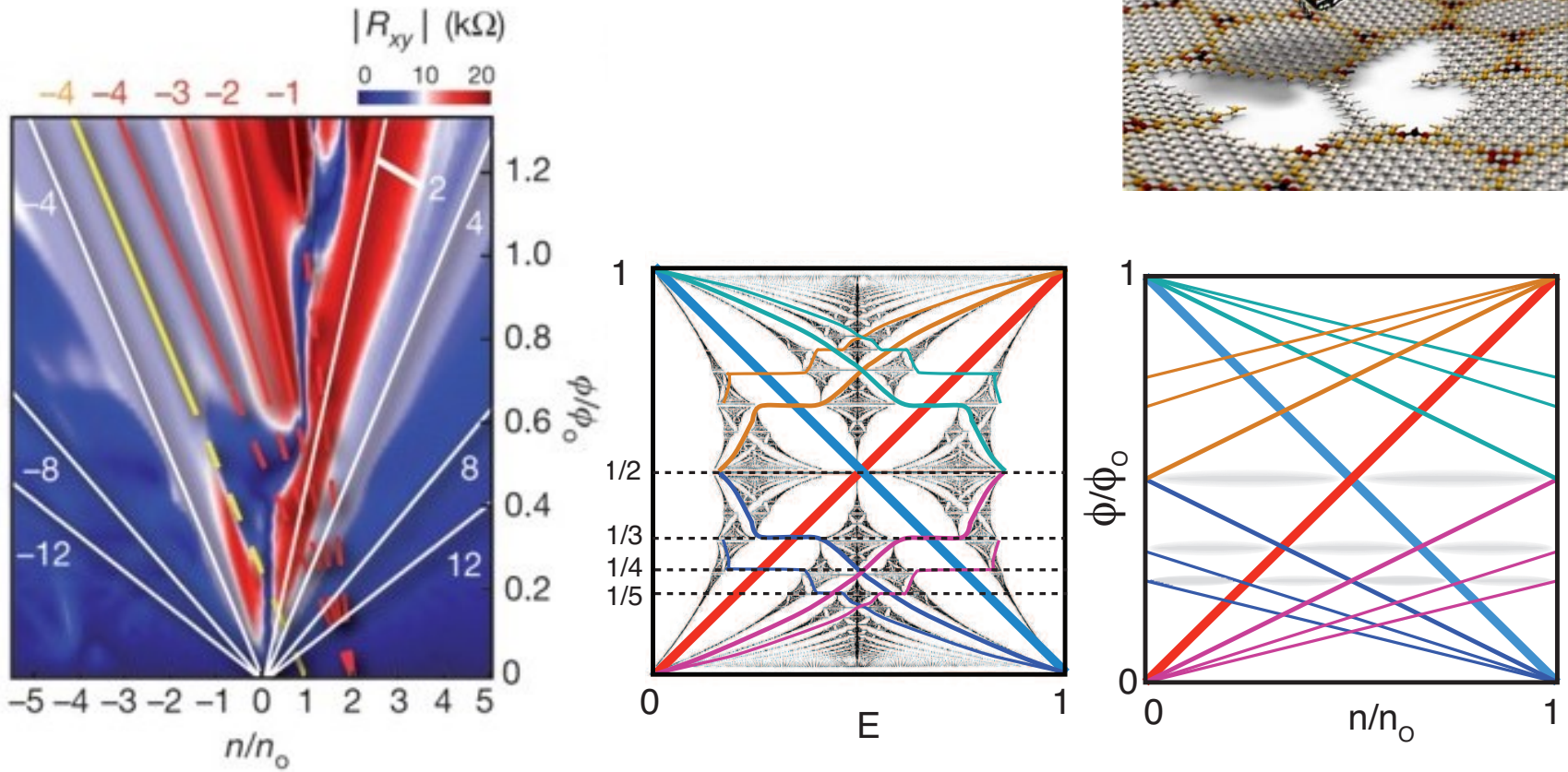

Figure: Moiré lattice constant $a_M = 15.5\,\text{nm}$ ($a = 0.25\,\text{nm}$). B $\approx 10^4 - 10^6\,G$. Electron density $n_0 = 1/A$ were A is area of moiré unit cell and n is integrated density of states.

Hofstadter's butterfly and the fractal quantum Hall effect in moiré superlattices, Dean, C. R.; Wang, L.; . . . ; Hone, J.; Kim, P. (30 May 2013). Nature. 497 (7451): 598–602.

Mechanical Relaxation

- When two layers are closely aligned, they form large-scale moiré patterns.
- This leads to atomistic relaxation on the moiré scale.
- Electronic properties depend on the relaxation.
- Incommensurate. Moiré patterns are not periodic on atomistic scale!

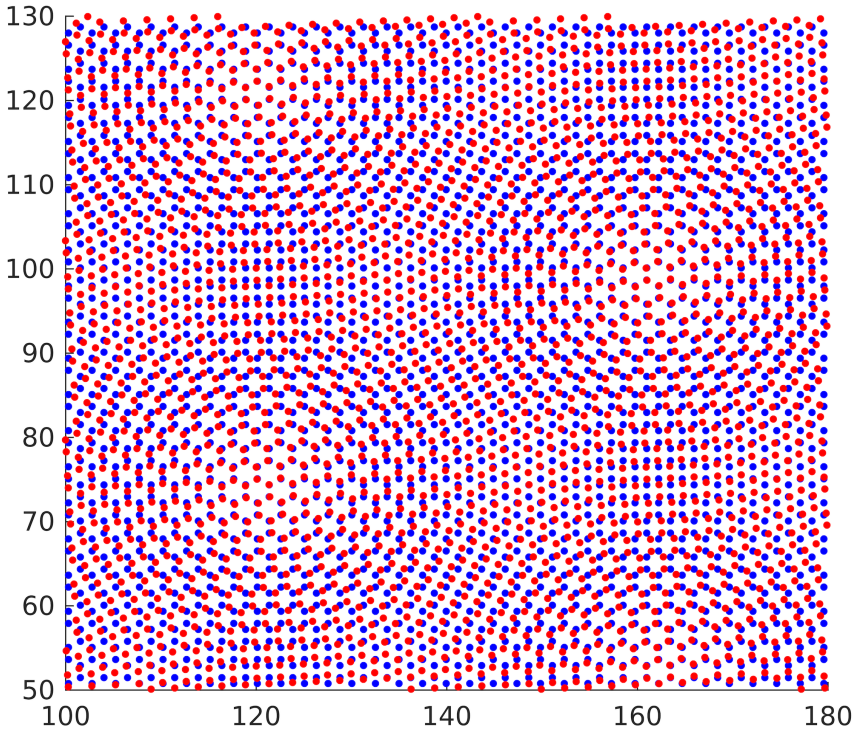

Unrelaxed

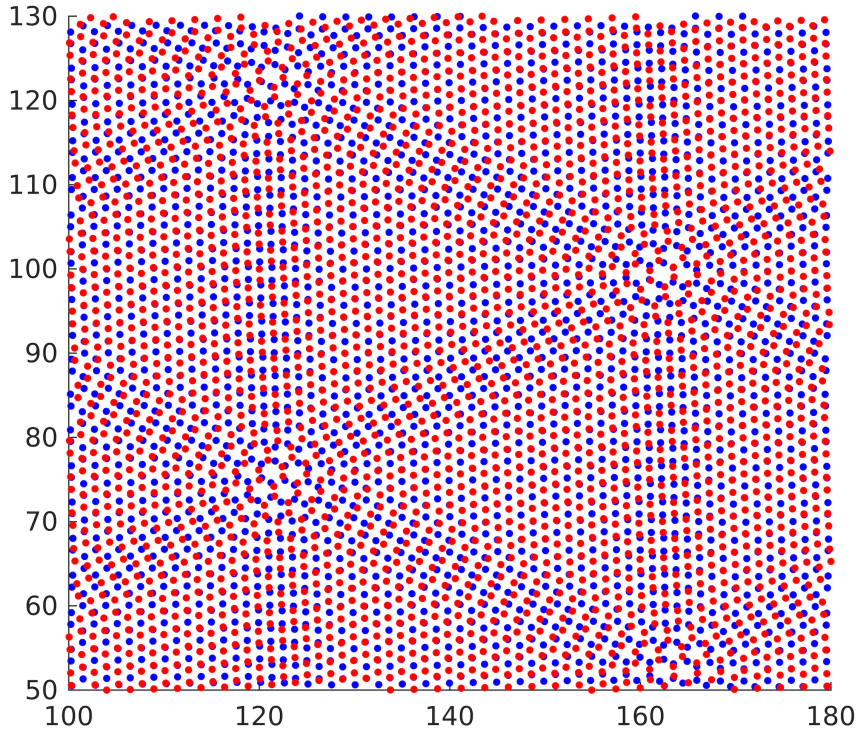

Relaxed

Energy minimization of 2D incommensurate heterostructures. Paul Cazeauz, Mitchell Luskin, and Daniel Massatt. Arch. Rat. Mech. Anal., 235:1289–1325, 2019.

Flat Band in Twisted Bilayer Graphene at Magic Angle

Flat Band $\Rightarrow$ Small Group Velocity $\frac{\partial \varepsilon}{\partial k}+$ Real Space Localization

Low Kinetic Energy $\Rightarrow$ Coloumb Energy $>$ Kinetic Energy.

Bistritzer-MacDonald (2011): Correlated phases such as superconductivity might exist due to electron-electron interactions?

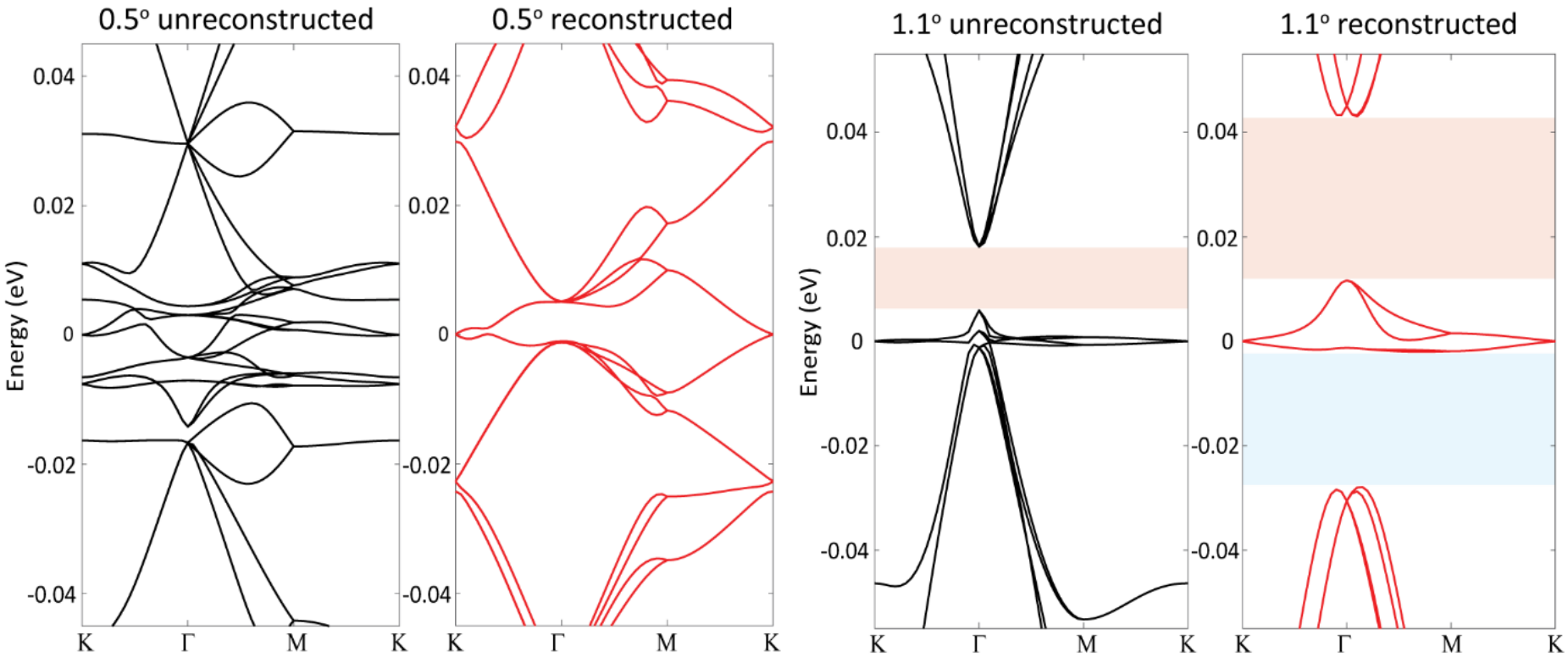

[*Atomic and electronic reconstruction at van der Waals interface in twisted bilayer graphene* , Hyobin Yoo, Rebecca Engelke, Stephen Carr, Shiang Fang,. . . , Mitchell Luskin, Ellad B. Tadmor, Efthimios Kaxiras, Philip Kim, *Nature Materials*, 2019]

Superconductivity and Mott Insulator States in Magic Angle TBG

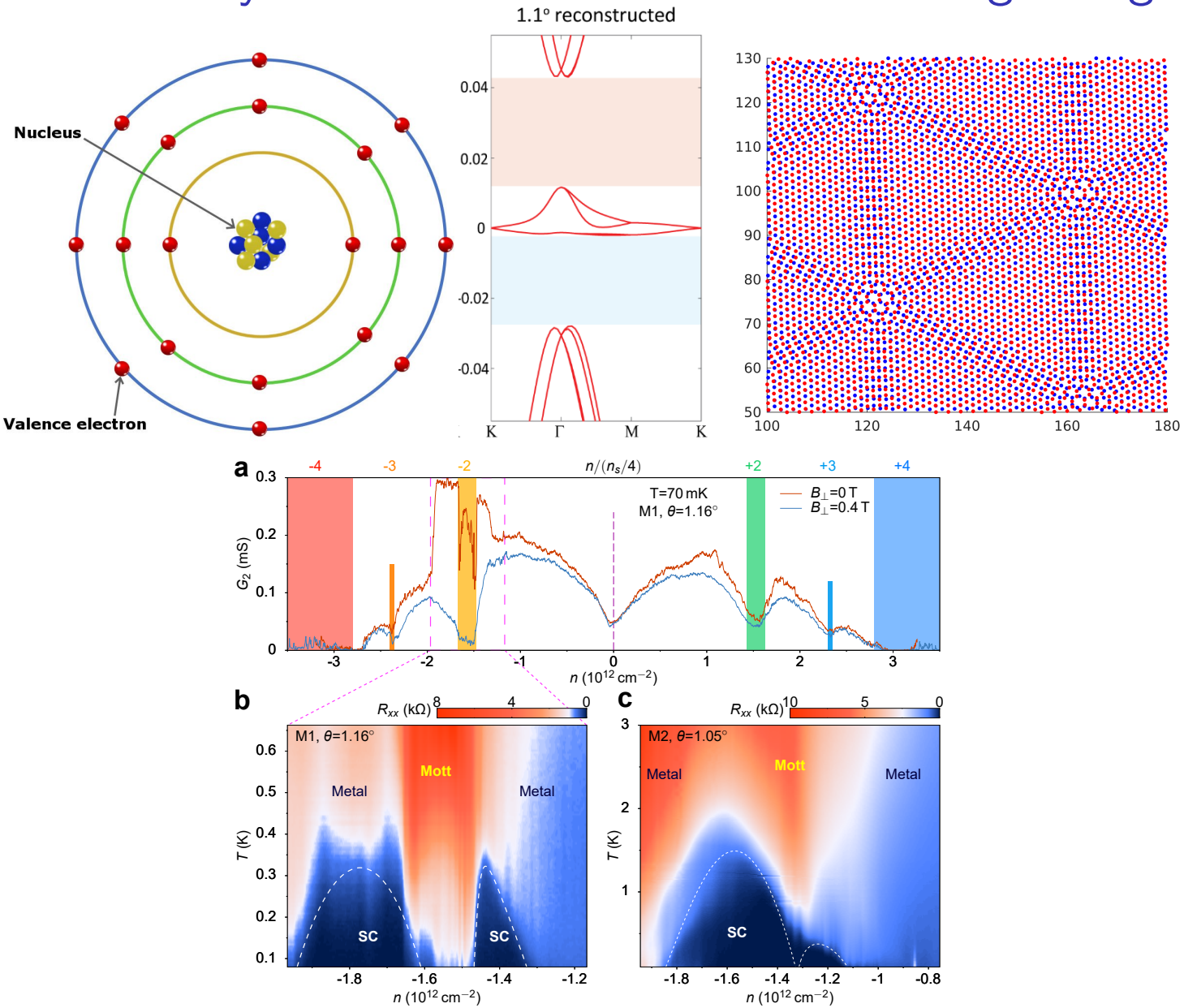

Unconventional superconductivity in magic-angle graphene superlattices, Yuan Cao, Valla Fatemi, Shiang Fang, & Pablo Jarillo-Herrero Nature volume 556, pages 43—50 (2018)

Real Space Localization of Electronic Density at Magic Angle

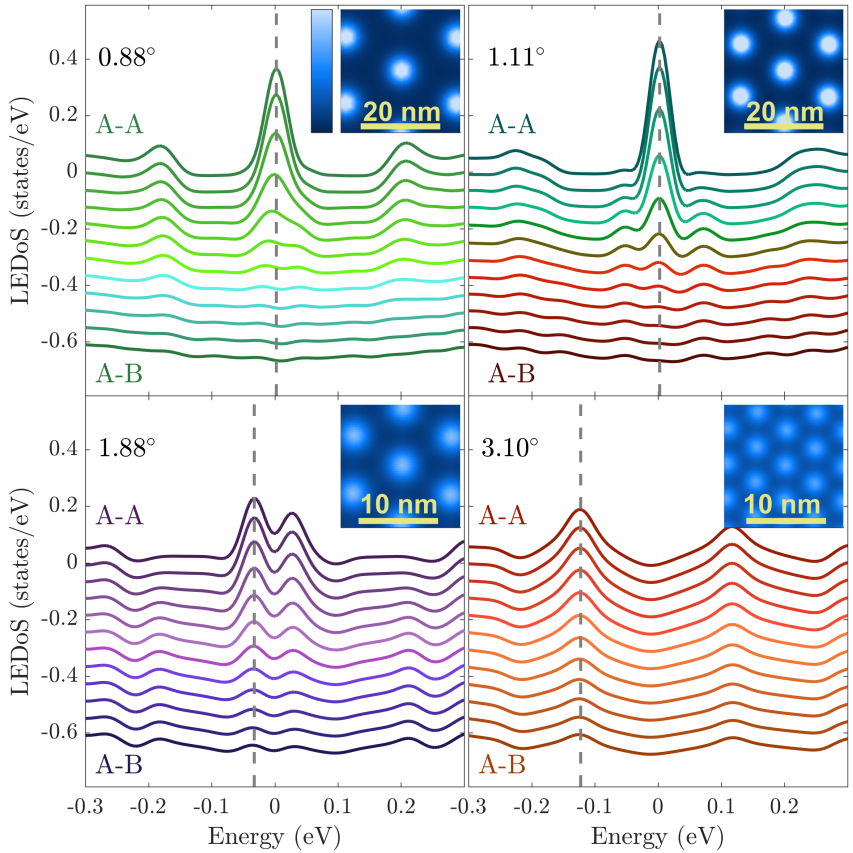

Figure: Simulated local electronic density of states (LEDoS) at four different angles of twisted bilayer graphene. The insets show a real-space image of the density of states in the bilayer system at the energy value identified by a dashed line.

[Twistronics: manipulating the electronic properties of two-dimensional layered structures through the twist angle, Stephen Carr, Daniel Massatt, Shiang Fang, Paul Cazeaux, Mitchell Luskin, and Efthimios Kaxiras. Nanoscale Phys. Rev. B, 95:075420, 2017.]

Library of moiré heterostructures with flat bands

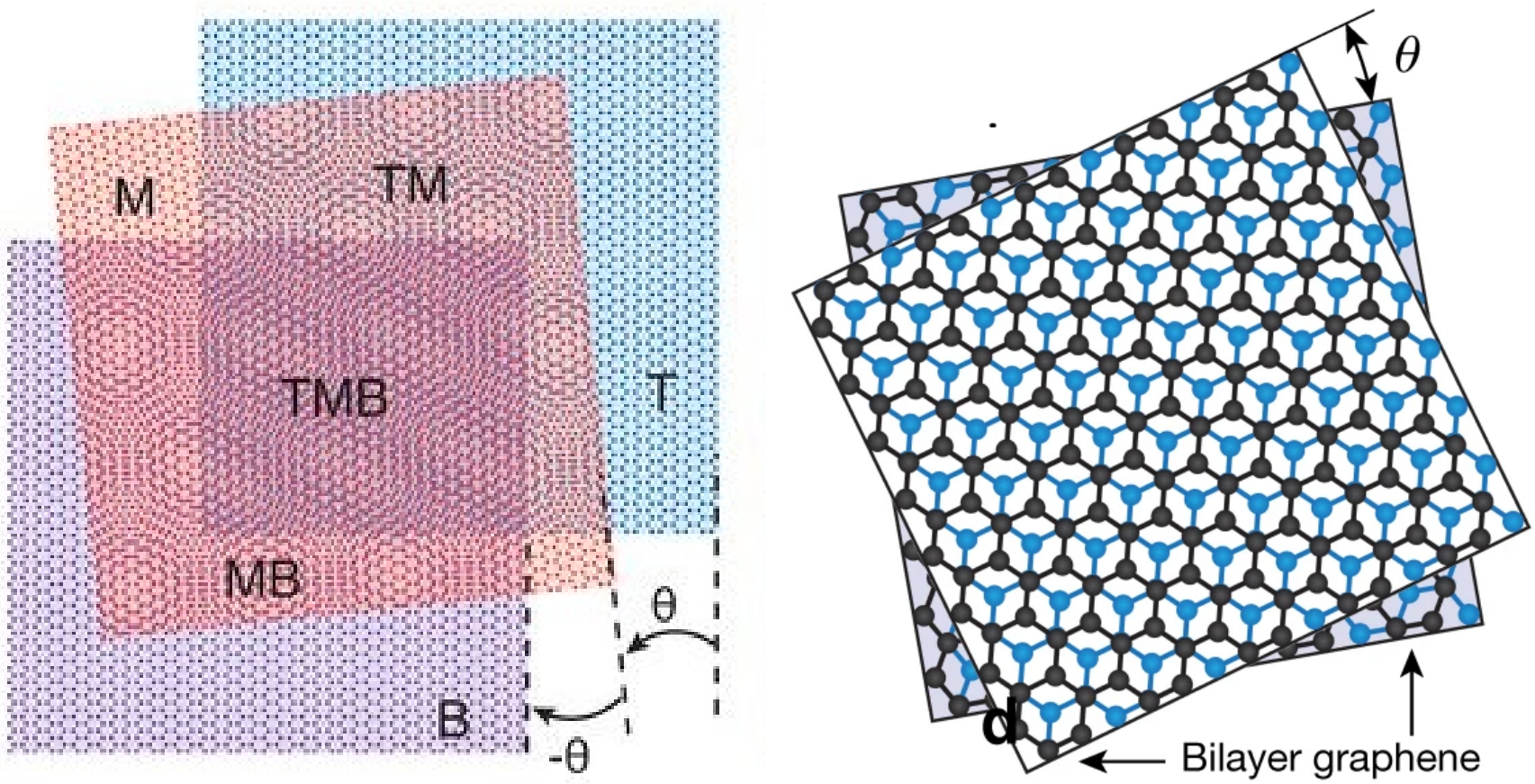

Figure: Left: Alternate-twist trilayer Gr. Right: Twisted double bilayer Gr.

Electric field–tunable superconductivity in alternating-twist magic-angle trilayer graphene, Zeyu Hao, A. M. Zimmerman, . . . Philip Kim, Science Mar 2021 : 1133-1138.
Liu, X., Hao, Z., Khalaf, E.,. . . P. Kim. Tunable spin-polarized correlated states in twisted double bilayer graphene. Nature 583, 221–225 (2020).

Library of moiré heterostructures with flat bands

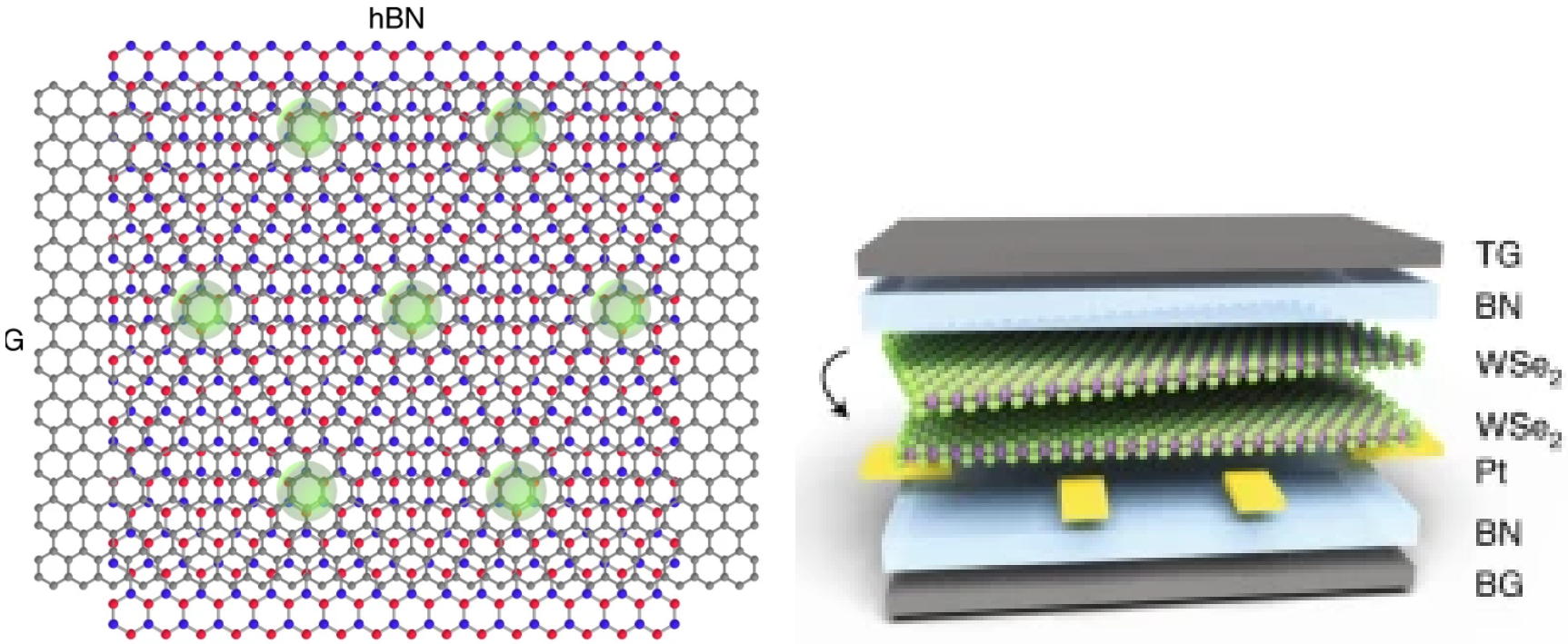

Figure: Left: ABC Trilayer Gr on hBN. Right: Twisted WSe_2 .

Chen, G., Jiang, L., Wu, et al. Evidence of a gate-tunable Mott insulator in a trilayer graphene moiré superlattice. Nat. Phys. 15, 237–241 (2019).
Wang, L., Shih, EM., Ghiotto, A., . . . , Dean, C. Correlated electronic phases in twisted bilayer transition metal dichalcogenides. Nat. Mater. 19, 861–866 (2020).

Periodic Table of Materials

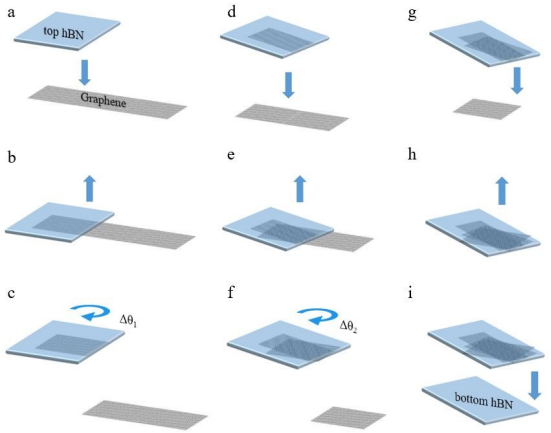

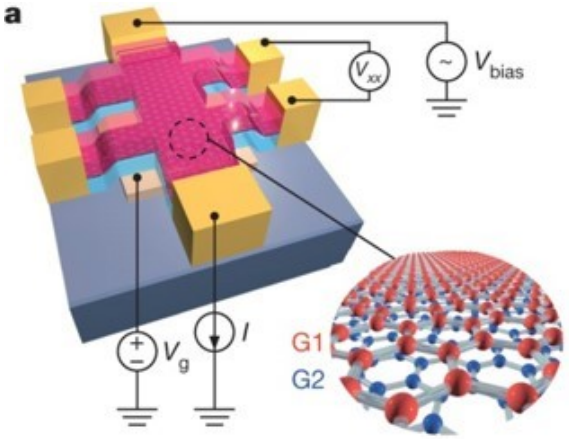

Can design Hamiltonian by tuning

- stacking order of 2D crystals
- moiré unit cell area by varying twist angle (tear and stack)
- filling of unit cell by varying gate voltage
- interlayer coupling strength by varying pressure
- electrical field
- magnetic field

Unconventional superconductivity without need to dope cuprates.

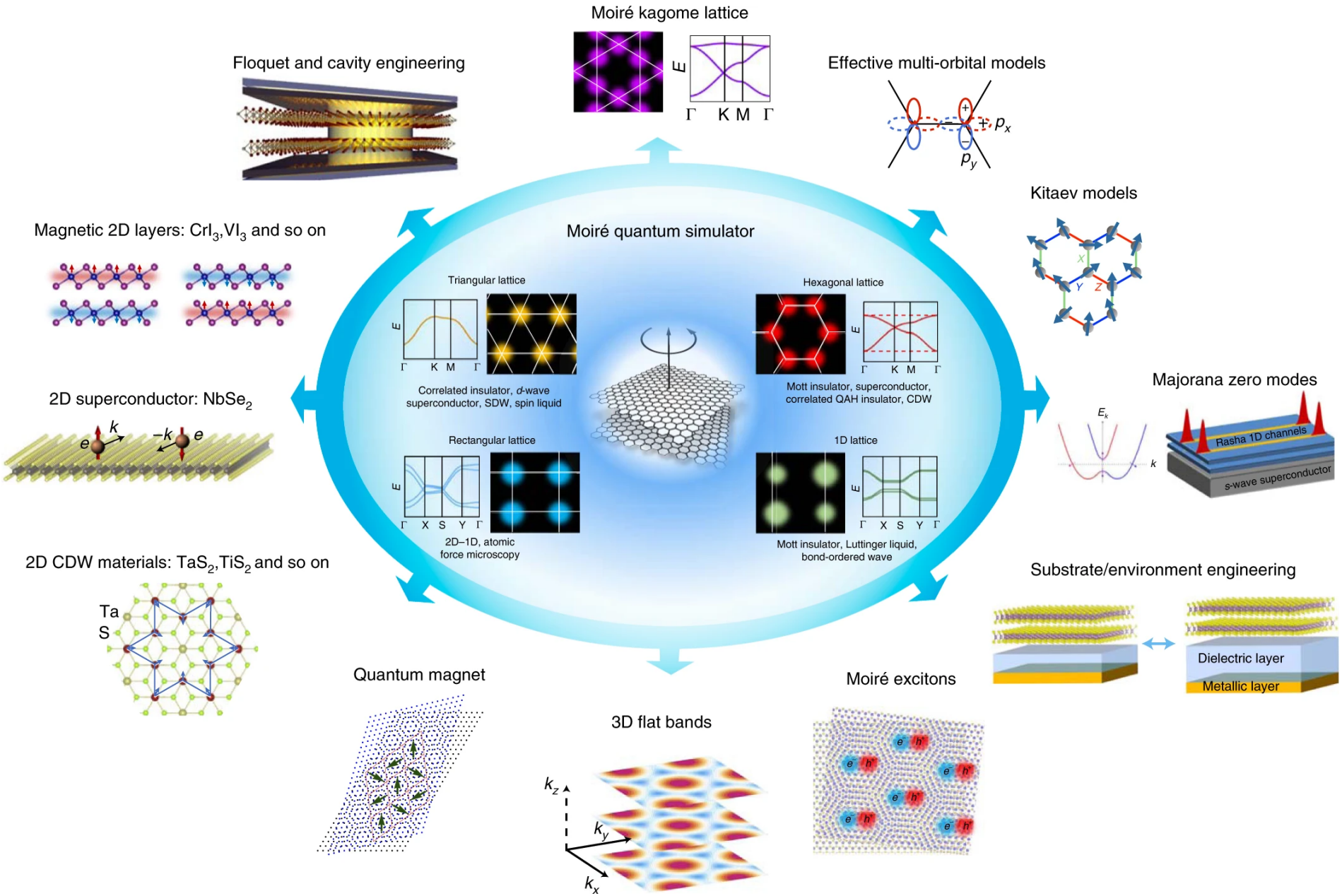

Moiré heterostructures as a Condensed-matter Quantum Simulator, D. Kennes, M. Claassen, . . . , J. Hone, C. Dean, D. N. Basov, A. N. Pasupathy & A. Rubio, Nature Physics, 17, pages 155–163 (2021).

Learning Band Structure

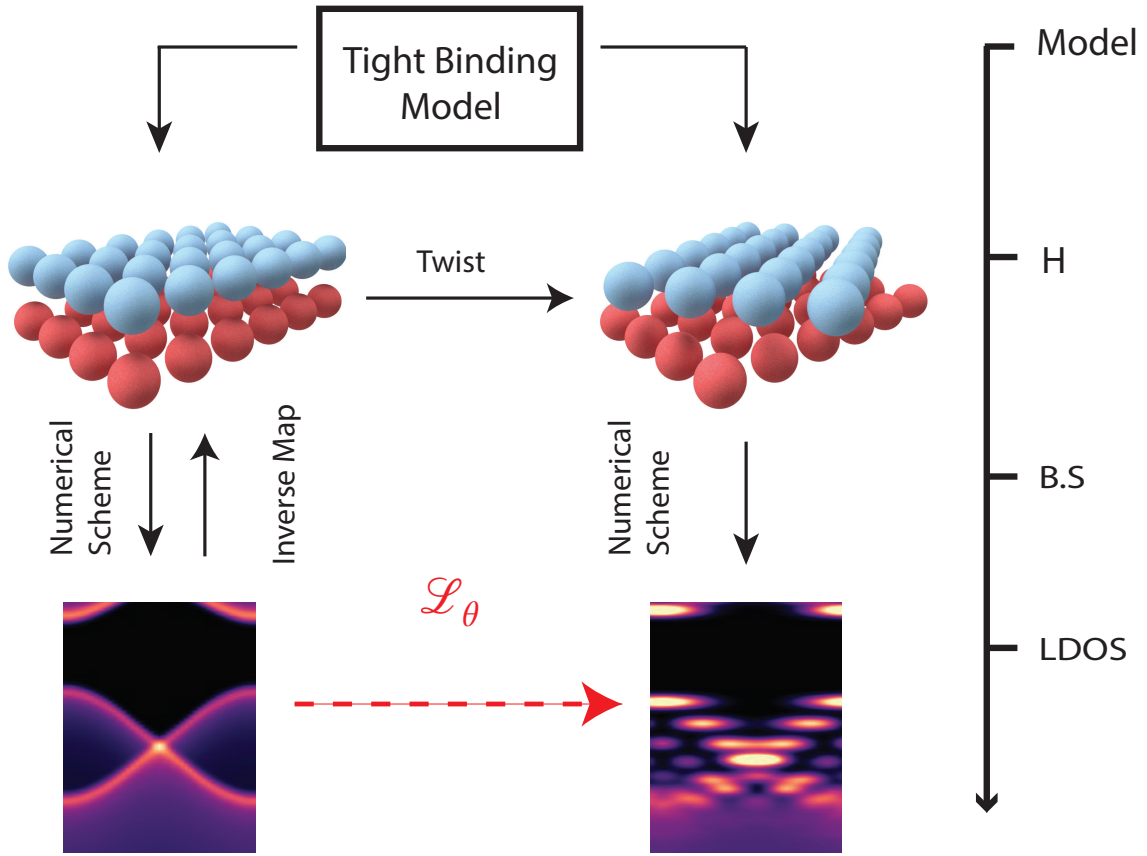

Figure: The $\mathcal{L}_\theta$ marked with the red dashed arrow is the image processing we aim to achieve, e.g., the Twist Operator to be learned with a neural network. The solid black arrows represent well-defined mappings.

Seeing moiré: convolutional network learning applied to twistronics. Diyi Liu, Mitchell Luskin, and Stephen Carr. Phys. Rev. Res., 4:043224 (11pp), 2022.

Learning Band Structure

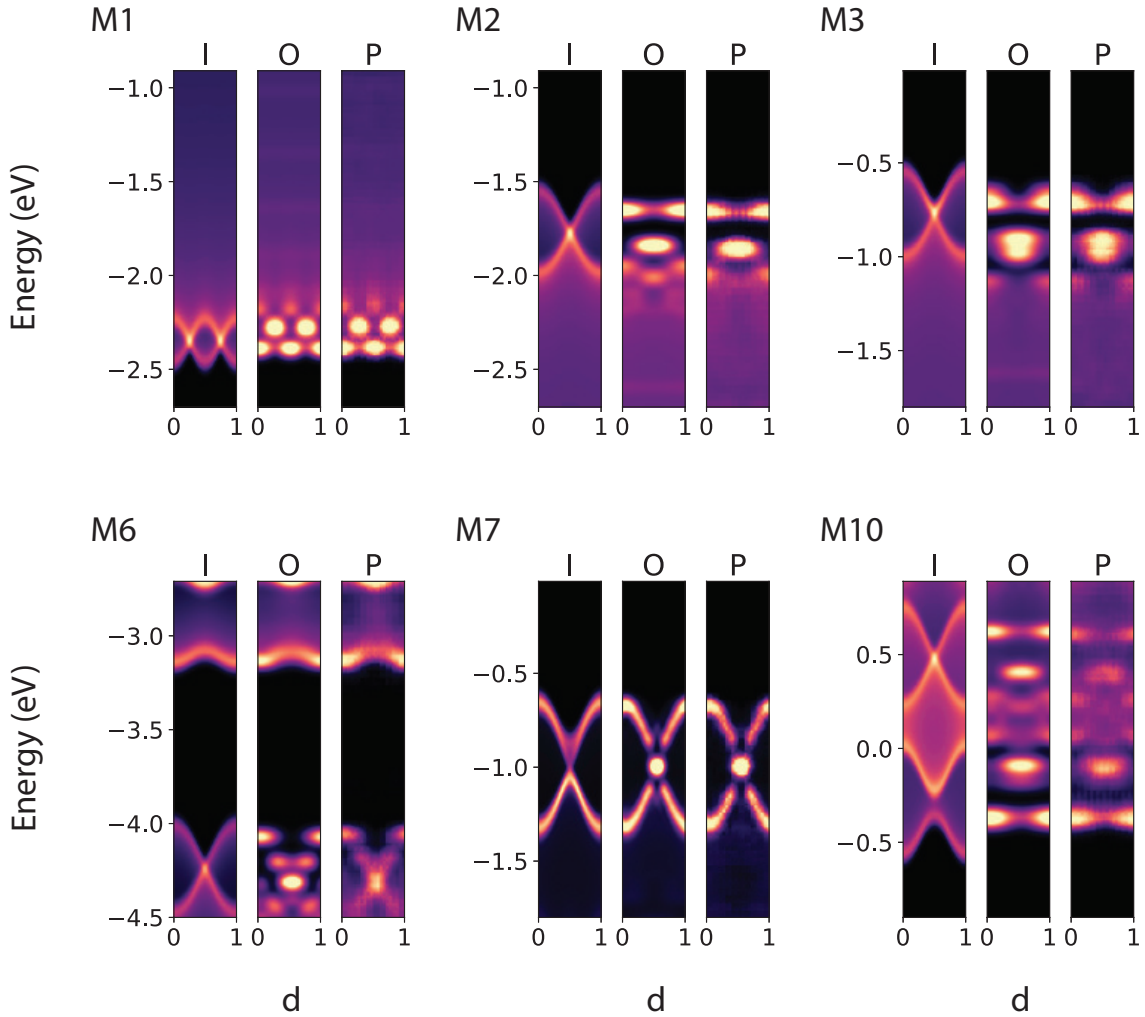

Figure: Comparison of configuration-dependent LDOS maps calculated from aligned bilayer Hamiltonians (input, I), moiré Hamiltonians (output, O), and predictions from our CNN (P) which are generated from the supplied input after training. Six representative cases are shown here, for bilayers of material types M1, M2, M3, M6, M7, and M10.

Reduced Models Needed for Correlated Physics

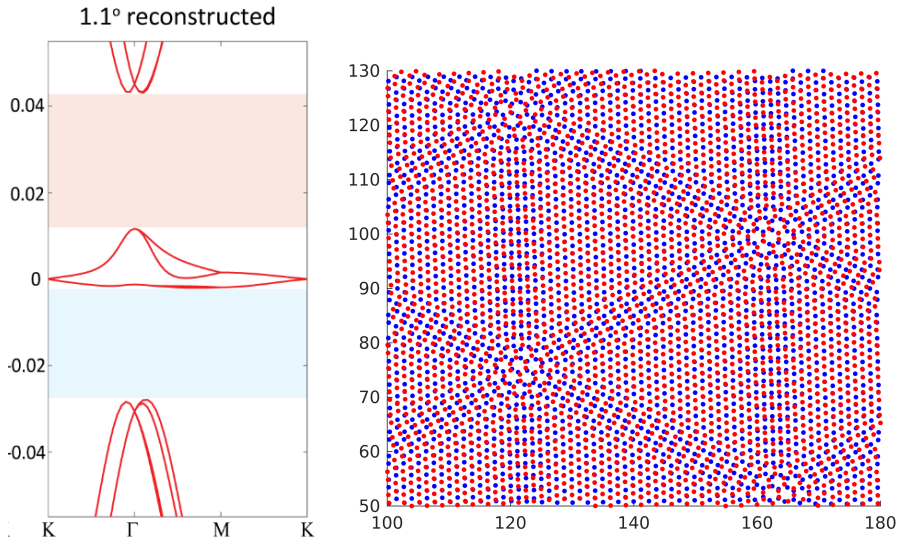

TBG moiré cell at magic angle $\theta = 1.05^\circ$: $10,000$ atoms, $60,000$ electrons.
Reference many-body model: Schrödinger equation for $\psi(x_1, \ldots, x_{60,000})$.

Can compute local density of states, band structure, Kubo conductivity, etc., from tight-binding approximation of single particle mean field Hamiltonian H (projection onto atomistic scale localized Wannier basis functions).

To study correlated physics, must solve

$$\hat{\boldsymbol{H}} = \sum_{p,\,q} t_{pq} \hat{\boldsymbol{a}}_p^+ \hat{\boldsymbol{a}}_q + \sum_{p,\,q,\,r,\,s} t_{pqrs} \hat{\boldsymbol{a}}_p^+ \hat{\boldsymbol{a}}_q^+ \hat{\boldsymbol{a}}_r \hat{\boldsymbol{a}}_s.$$

Moiré scale Wannier functions

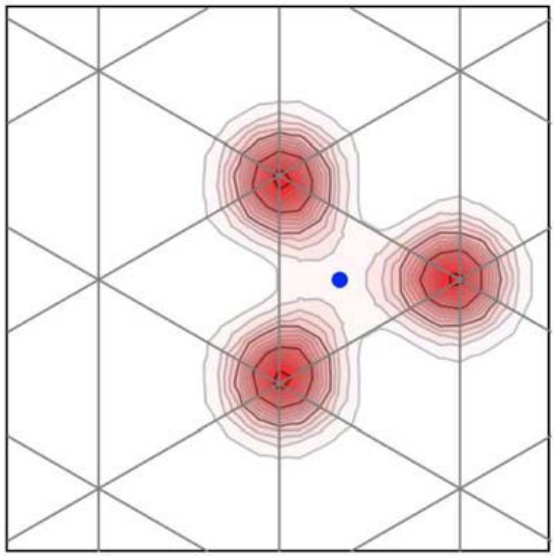

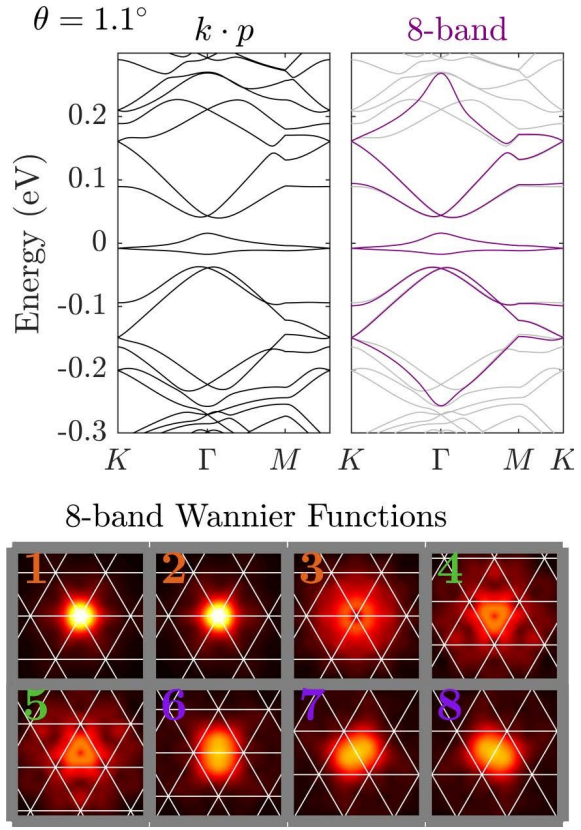

$$\hat{H} = \sum_{p,q} t_{pq} \hat{a}_p^+ \hat{a}_q + \sum_{p,q,r,s} t_{pqrs} \hat{a}_p^+ \hat{a}_q^+ \hat{a}_r \hat{a}_s .$$

Reduced models: Project onto flat bands. 8 localized (at moiré scale) Wannier basis functions per moiré cell versus $10,000$. Topological obstructions? Fragile topology.

Mikito Koshino, ..., and Liang Fu Phys. Rev. X 8, 031087, 2018,
Stephen Carr, S. Fang, H. Po, A. Vishwanath, and E. Kaxiras Phys. Rev. Research 1, 033072, 2019.

Bistritzer-MacDonald model

Bistritzer-MacDonald (2011) proposed to model electrons in twisted bilayer graphene by a moiré-periodic PDE model

$$i\partial_t \psi = H_{\mathrm{BM}}\psi, \quad H_{\mathrm{BM}} := \begin{pmatrix} \vec{\sigma}\cdot(-i\vec{\nabla}) & T(\vec{r}) \\ T^\dagger(\vec{r}) & \vec{\sigma}\cdot(-i\vec{\nabla}) \end{pmatrix},$$

where $\psi(t)$ the wave-function of an electron, $\vec{\sigma} = (\sigma_1, \sigma_2)$ the vector of Pauli matrices, and $T(\vec{r})$ a moiré-periodic potential

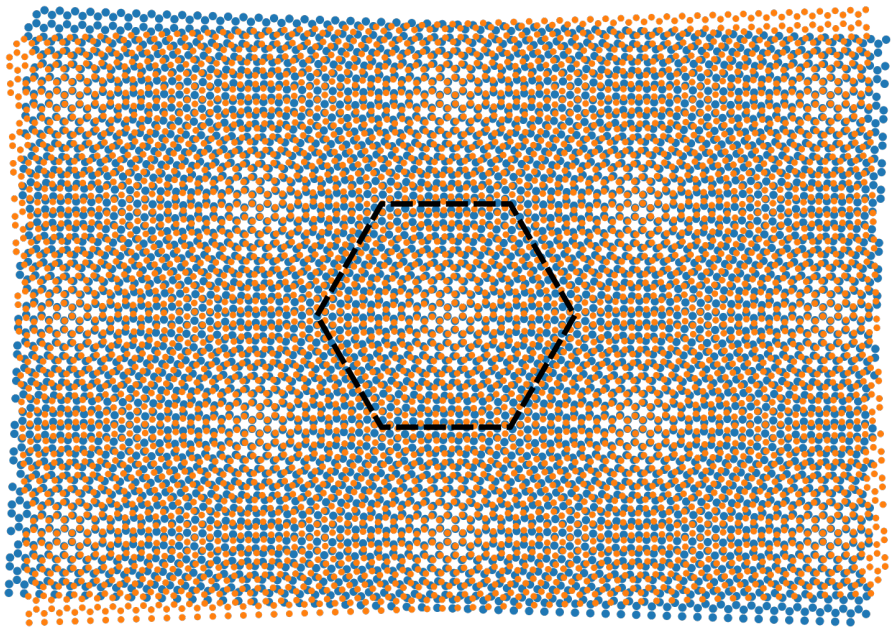

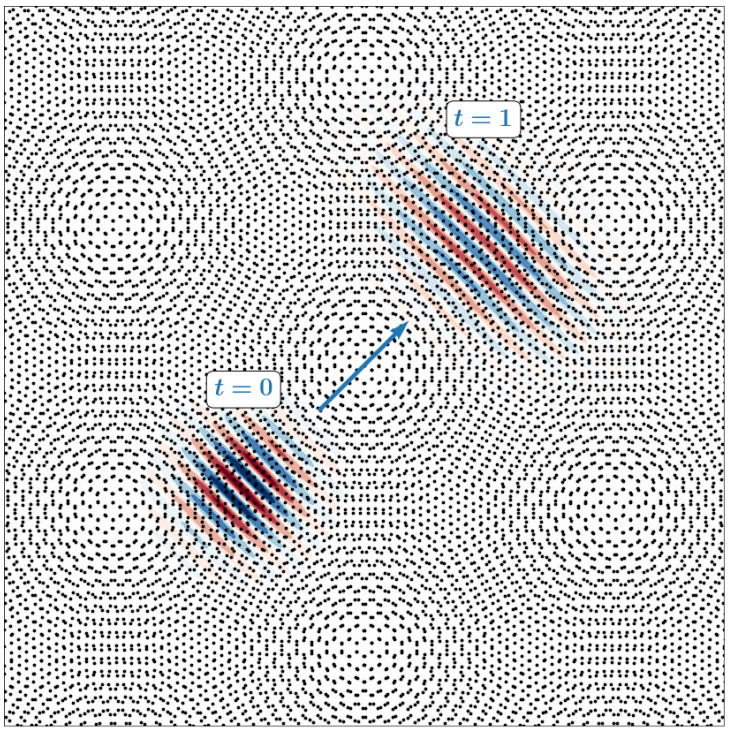

Main theorem

Theorem (Watson-Kong-MacDonald-Luskin 2022 [simplified])

Consider the tight-binding model of twisted bilayer graphene $i\partial_t\psi = H\psi$, *with wave-packet initial data* $\psi(0) = \epsilon f_0(\epsilon\vec{R})e^{i\vec{K}_i\cdot\vec{R}}$ *localized at Dirac point* $\vec{K}_i$ *in layer* i, *with spectral width* $\epsilon \ll 1$.

Suppose the interlayer hopping function h *satisfies the assumption, and* ℓ *and* θ *satisfy*

$$|\hat{h}(|\vec{K}|;\ell)| \sim \epsilon, \quad \theta \lesssim \epsilon.$$

Then, $\psi(t) = \epsilon f(\epsilon\vec{R}, \epsilon t)e^{i\vec{K}_i\cdot\vec{R}} + O_{\ell^2}(\epsilon^2 t)$ *evolves as wave-packet up to* $t \sim \epsilon^{-2+\delta}$ *(any* $\delta > 0$*), with envelopes* $f = (f_1^A, f_1^B, f_2^A, f_2^B)^\top$ *modulated by*

$$i\partial_T f = H_{BM} f, \quad H_{BM} := \begin{pmatrix} \vec{\sigma}\cdot(-i\vec{\nabla}) & T(\vec{r}) \\ T^\dagger(\vec{r}) & \vec{\sigma}\cdot(-i\vec{\nabla}) \end{pmatrix},$$

$\vec{\sigma} = (\sigma_1, \sigma_2)$ *vector of Pauli matrices,* $T(\vec{r})$ *moiré potential.*

Bistritzer-MacDonald dynamics in twisted bilayer graphene. A. Watson, T. Kong, A. H. MacDonald, and M. Luskin. J. Math. Phys. 64:031502 (38pp), 2023

Veselago Lens and Klein Collimater

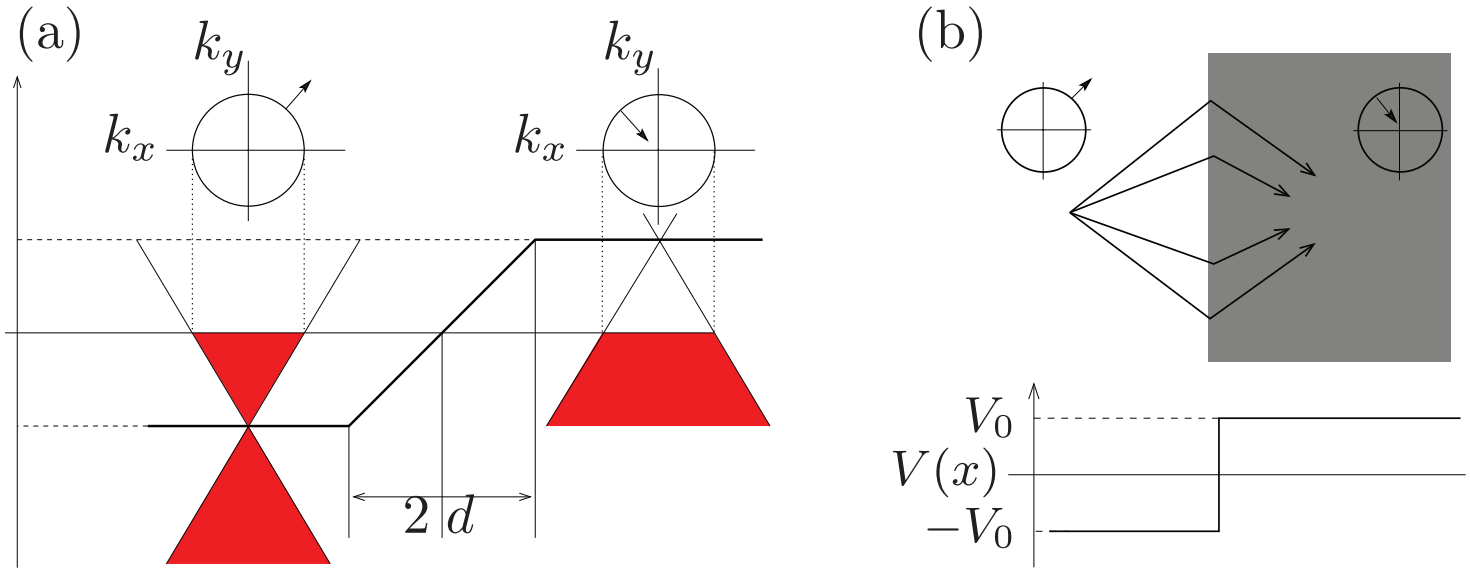

[*Veselago lens and Klein collimator in disordered graphene*, F Libisch, T Hisch1, R Glattauer, L A Chizhova1 and J Burgdörfer, J. Phys.: Condens. Matter, , 2017]

Gate-tunable Veselago Interference in a Bipolar Graphene Microcavity

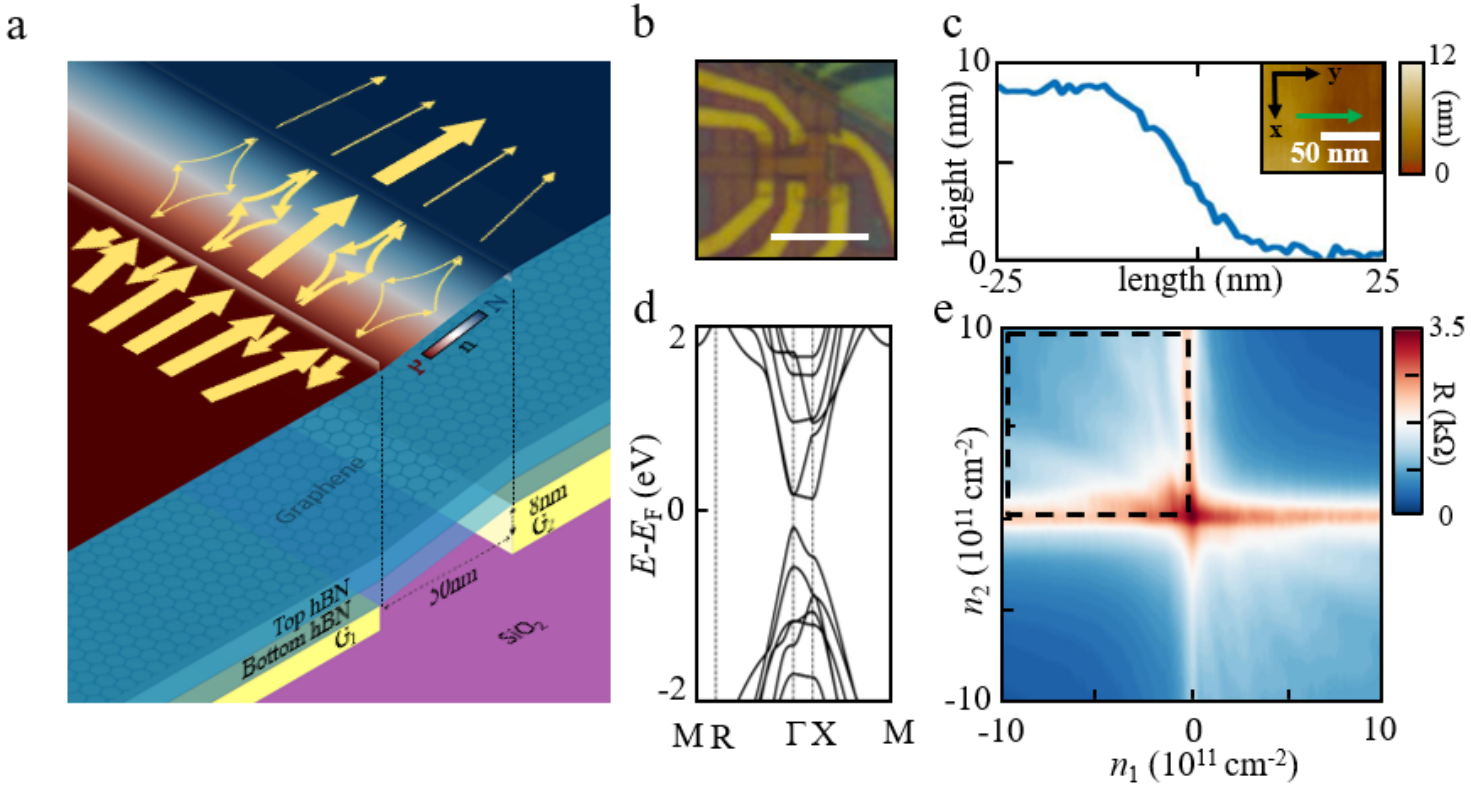

[*Gate-tunable Veselago Interference in a Bipolar Graphene Microcavity*, X. Zhang, W. Ren,. . . , E. Kaxiras, M. Luskin, K. Wang, Nature Communications, 13:6711 (7pp)(18pp supplementary material), 2022.]

2D bilayer geometry

For layers $j \in \{1, 2\}$, we define the Bravais lattice

$$\mathcal{R}_j = \{A_j n : n \in \mathbb{Z}^2\}$$

where A_j is a 2×2 invertible matrix whose columns are primitive lattice vectors. We define the *unit cell* for layer j as

$$\Gamma_j = \{A_j x : x \in [0, 1)^2\}.$$

Reciprocal lattice: $\mathcal{R}_j^* := \{2\pi A^{-T} n : n \in \mathbb{Z}^2\}$.
Brillouin Zone: $\Gamma_j^* := BZ_j := \{2\pi A_j^{-T} x : x \in [0, 1)^2\}$.

Represent multilattices by $\mathcal{R}_1 \times \mathcal{A}_1$ and $\mathcal{R}_2 \times \mathcal{A}_2$
where $\mathcal{A}_i$ denotes the set of orbitals associated with each lattice point in layer i.

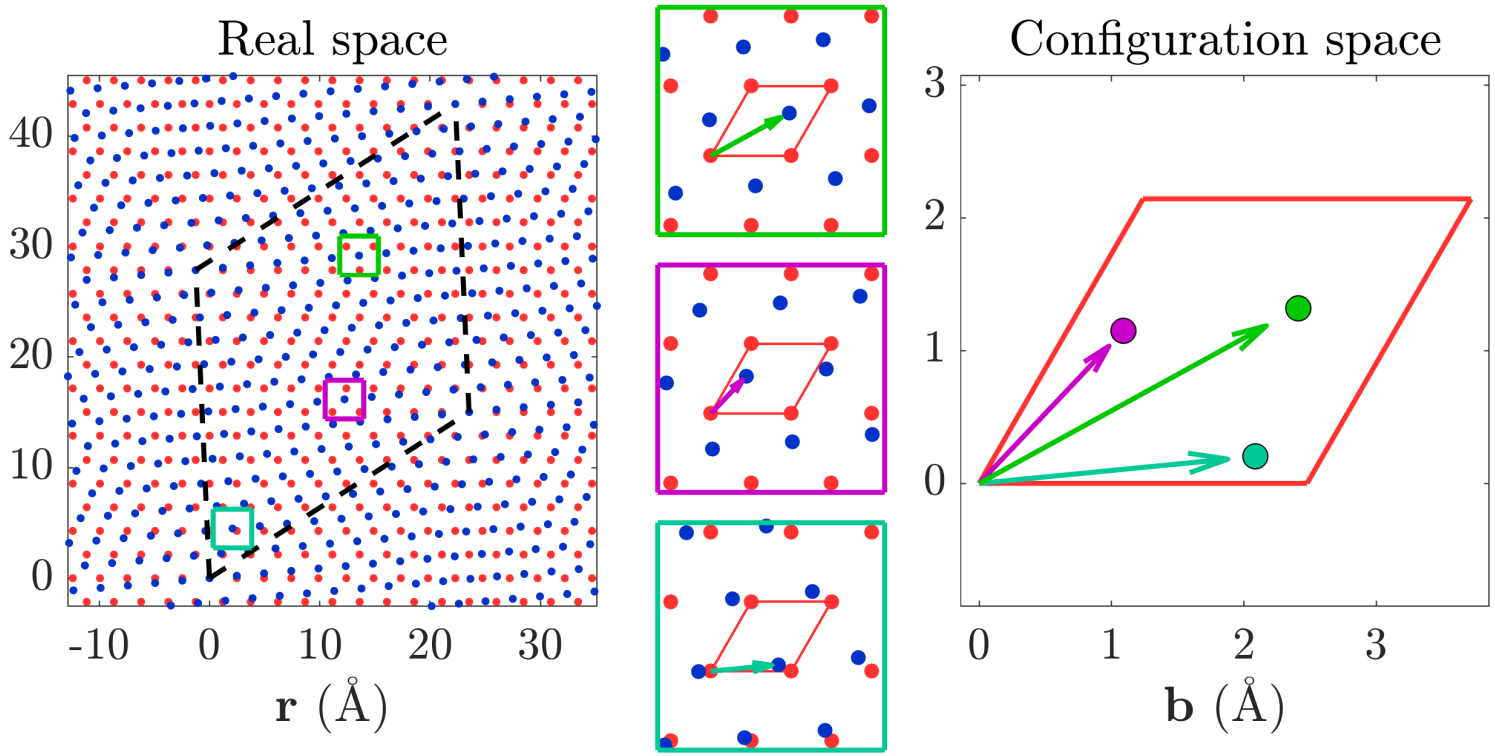

Blue lattice points' ($\mathcal{R}_1$) local environment (Γ_2) described completely by the disregistry between the red and blue unit-cells.

Isomorphism (one-to-one mapping) between $\mathcal{R}_1$ and configurations (disregistries) (Γ_2) of incommensurate systems.

Configuration space approach gives a unified theoretical and computational approach to mechanics, electronic structure, transport, and diffraction.

Disregistry

The disregistry of an atom R_1 of layer 1 with respect to layer 2 is given by

$$b_{1\to 2}(R_1) = \mathrm{mod}_{\Gamma_2}(R_1), \qquad R_1 \in \mathcal{R}_1.$$

Since $A_2 A_1^{-1} R_1 \in \mathcal{R}_2$, we can smoothly interpolate to $\mathbb{R}^2$ by

$$b_{1\to 2}(x) = \mathrm{mod}_{\Gamma_2}\left[(I - A_2 A_1^{-1})x\right].$$

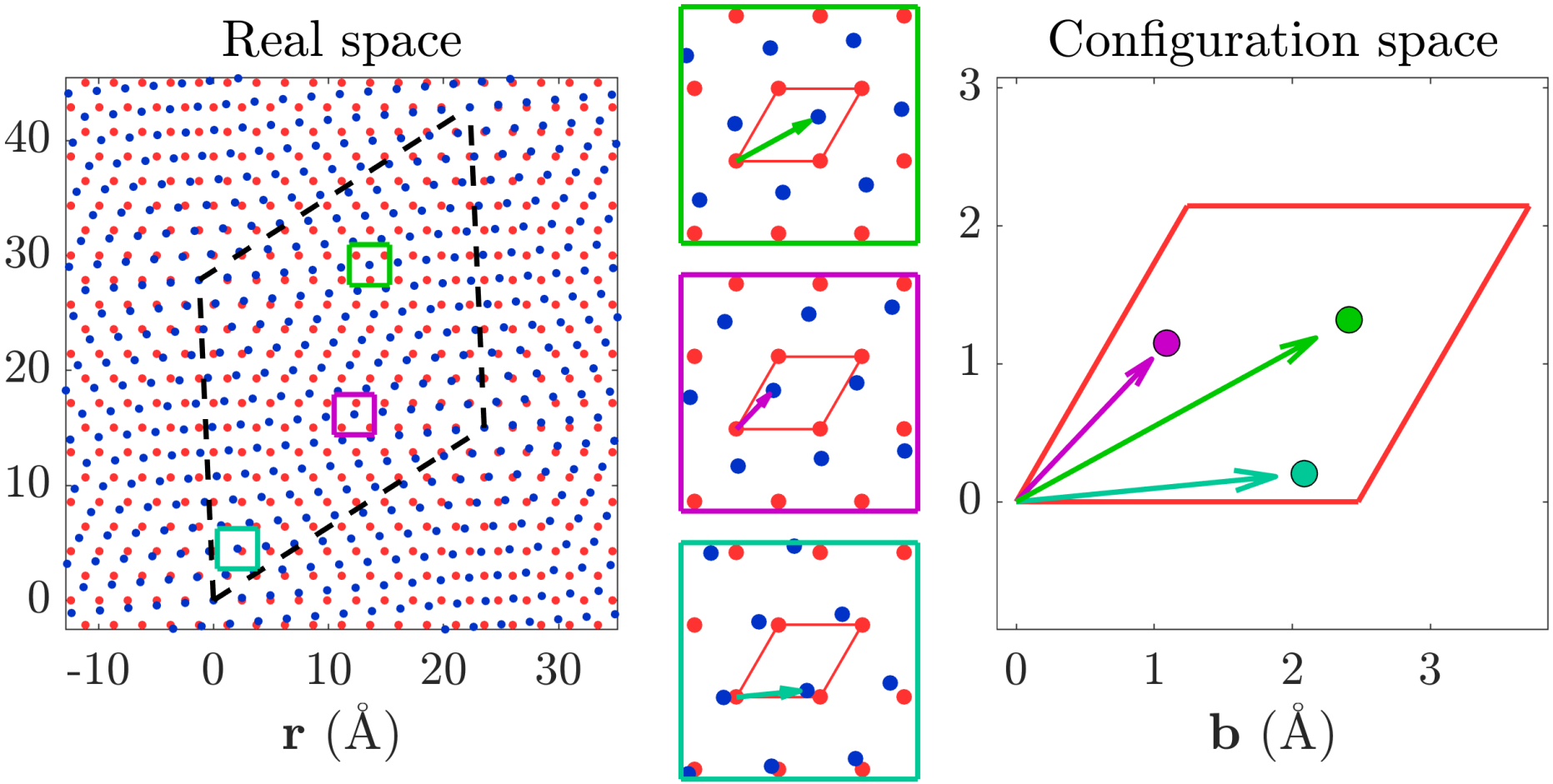

Moiré Unit Cell and Superlattice

$b_{1\to 2}(x)$ and $b_{2\to 1}(x)$ are isomorphisms

$$b_{1\to 2}: \begin{cases} \Gamma_{\mathcal{M}} \to \Gamma_2, \\ \quad x \mapsto (I - A_2 A_1^{-1})x = A_2(A_2^{-1} - A_1^{-1})x, \end{cases}$$

$$b_{2\to 1}: \begin{cases} \Gamma_{\mathcal{M}} \to \Gamma_1, \\ \quad x \mapsto (I - A_1 A_2^{-1})x = A_1(A_1^{-1} - A_2^{-1})x, \end{cases}$$

where $\Gamma_{\mathcal{M}}$ is the periodic moiré cell:

$$\Gamma_{\mathcal{M}} := \mathbb{R}^2/\mathcal{R}_{\mathcal{M}} \equiv (A_1^{-1} - A_2^{-1})^{-1}[0,1)^2,$$

and $\mathcal{R}_{\mathcal{M}}$ is the moiré superlattice given by

$$\mathcal{R}_{\mathcal{M}} := (A_1^{-1} - A_2^{-1})^{-1}\mathbb{Z}^2.$$

Reciprocal moiré lattice is then given by

$$\mathcal{R}^*_{\mathcal{M}} := 2\pi(A_1^{-T} - A_2^{-T})\mathbb{Z}^2.$$

Ergodicity of Disregistries for Incommensurate 2D Layers

For $h \in C_{\text{per}}(\Gamma_2)$, we thus have that $h(R_1) = h(b_{1\to 2}(R_1))$ and

$$\frac{1}{\#\mathcal{R}_1 \cap B_r} \sum_{R_1 \in \mathcal{R}_1 \cap B_r} h(R_1) = \frac{1}{\#\mathcal{R}_1 \cap B_r} \sum_{R_1 \in \mathcal{R}_1 \cap B_r} h(b_{1\to 2}(R_1)) \to \frac{1}{|\Gamma_2|} \int_{\Gamma_2} h(b)db.$$

Replace integrals (traces) over $BZ_{\text{supercell}}$ by disregistries Γ_2

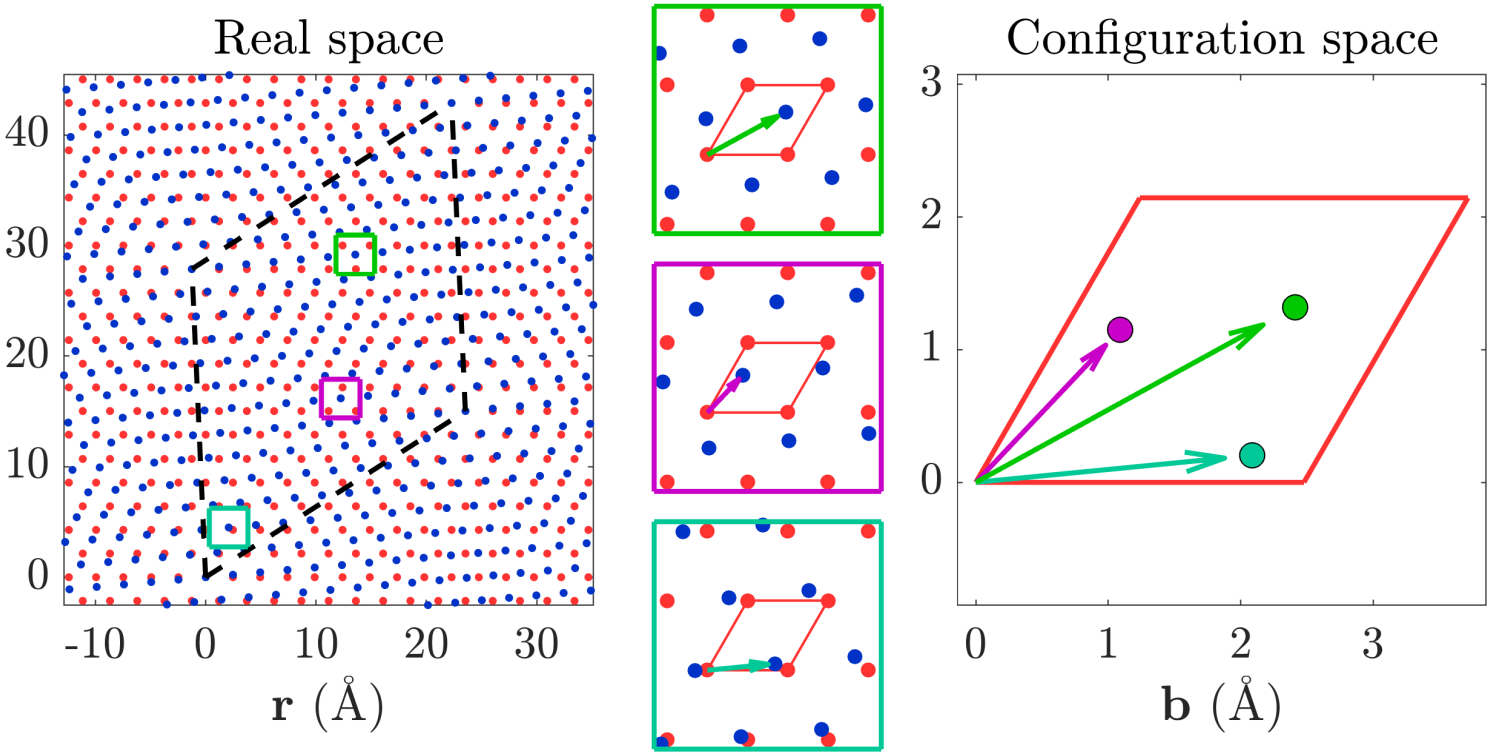

Generalized Kubo formulas for the transport properties of incommensurate 2D atomic heterostructures. E. Cancés, P. Cazeaux, and M. Luskin. Journal of Mathematical Physics, 58:063502, 2017.

Electronic density of states for incommensurate layers. Daniel Massatt, Mitchell Luskin, and Christoph Ortner. SIAM J. Multiscale Modeling & Simulation, 15:476–499, 2017.

Density of States for Lattice by Trace (Integral) over BZ

The density of states $\rho(E)$ can be computed by the formula

$$\rho(E) = \sum_{m=1}^{|\mathcal{A}|} \int_{\Gamma^*} \delta(\varepsilon_m(q) - E)\, dq = \sum_{m=1}^{|\mathcal{A}|} \int_{\varepsilon_m(q)=E} \frac{d\ell}{|\nabla_q \varepsilon_m(q)|},$$

where $d\ell$ is the line integral on the level sets of the bands $\varepsilon_m(q) = E$ since $dq = |\nabla_q \varepsilon_m(q)|^{-1}\, d\varepsilon_m\, d\ell$.

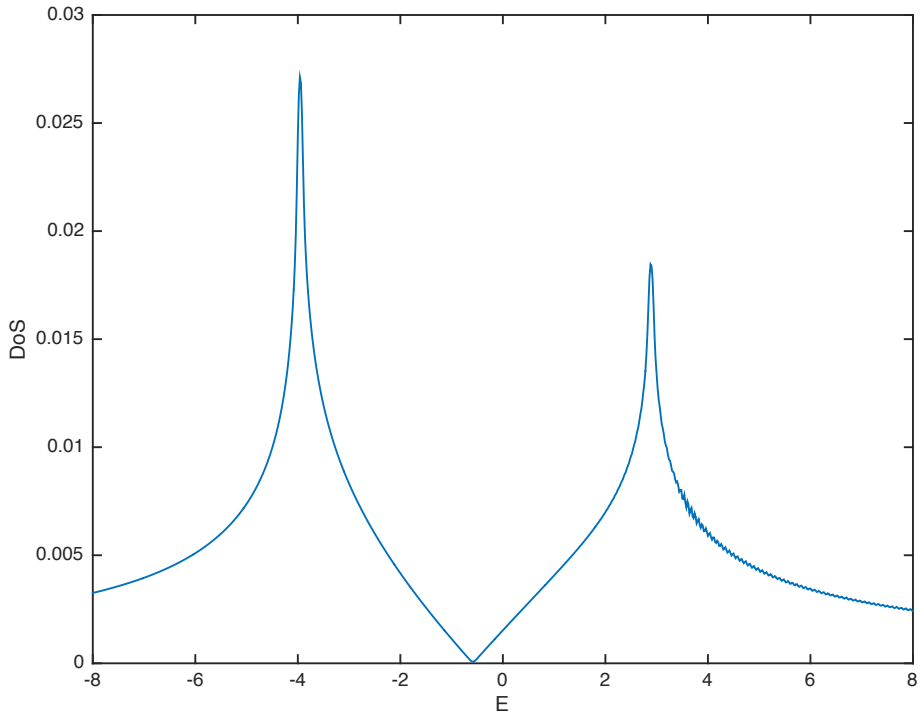

Figure: Linear DoS at Fermi Level and Van Hove singularity.

Density of States for Incommensurate 2D Layers

We have that

$$\mathcal{D}_{R\alpha}[H] \approx \mathcal{D}_{0\alpha}[H_1(b_{1\to 2}(R_1))], \quad R_1\alpha_1 \in \mathcal{R}_1 \times \mathcal{A}_1,$$

where $\mathcal{D}_{R_1\alpha_1}[H]$ is the local density of states at $R_1\alpha_1 \in \mathcal{R}_1 \times \mathcal{A}_1$, and $H_1(b_2)$ is the Hamiltonian with layer 2 shifted by disregistry $b_2 \in \Gamma_2$.

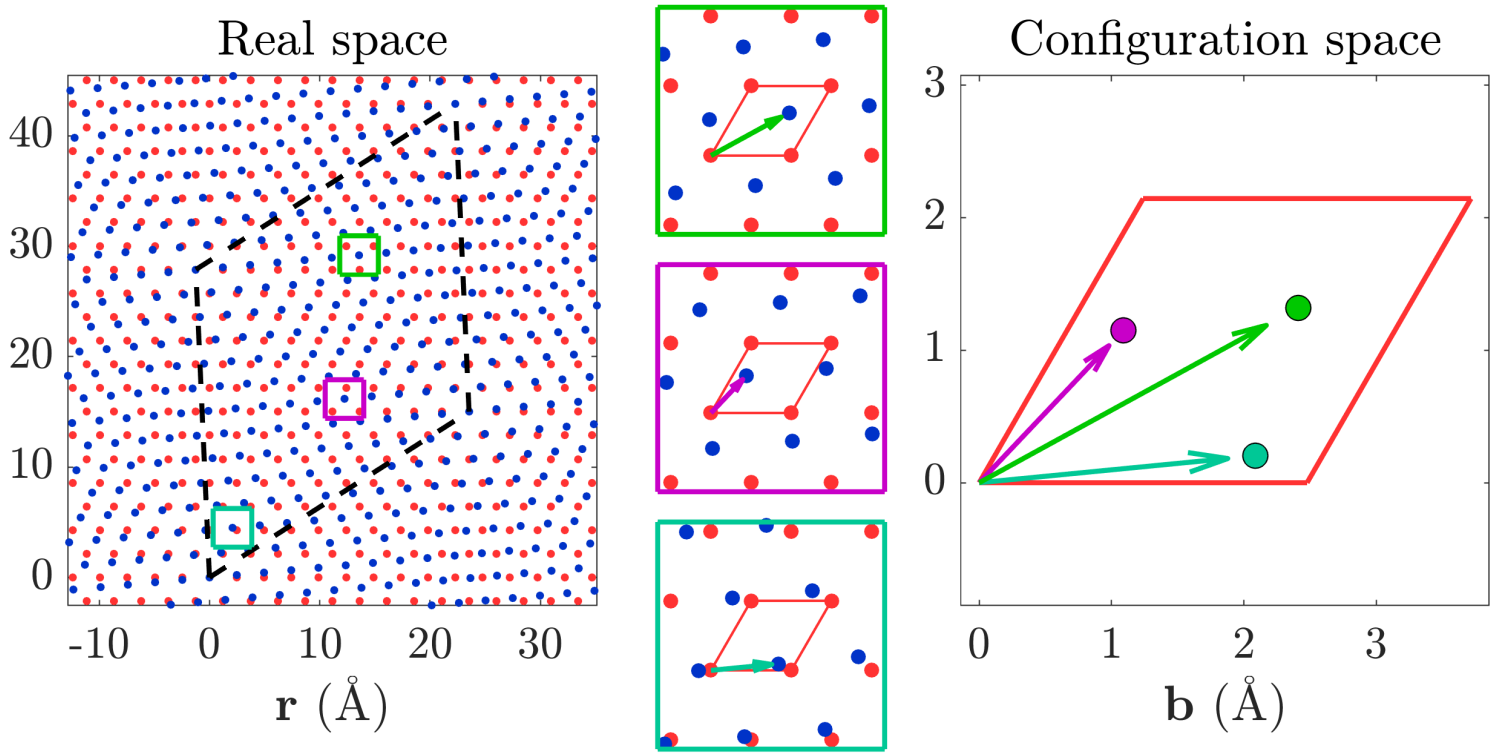

Density of States for Incommensurate 2D Layers

Since

$$\mathcal{D}_{R_1\alpha_1}[H] \approx \mathcal{D}_{0\alpha_1}[H_j(b_{1\to 2}(R_1))], \quad R_1\alpha_1 \in \mathcal{R}_1 \times \mathcal{A}_1,$$

and $b_{1\to 2}(R_1)$ for $R_1 \in \mathcal{R}_1$ uniformly samples Γ_2, we can rigorously derive the ergodic property for the local density of states of incommensurate lattices

$$\begin{aligned}
&\frac{1}{\#\{\mathcal{R}_1 \times \mathcal{A}_1\} \cap B_r} \sum_{R_1\alpha_1 \in \{\mathcal{R}_1 \times \mathcal{A}_1\} \cap B_r} \mathcal{D}_{R_1\alpha_1}[H] \\
&\approx \frac{1}{\#\{\mathcal{R}_1 \times \mathcal{A}_1\} \cap B_r} \sum_{R_1\alpha_1 \in \{\mathcal{R}_1 \times \mathcal{A}_1\} \cap B_r} \mathcal{D}_{0\alpha_1}[H_1(b_{1\to 2}(R_1))] \\
&\to \frac{1}{|\mathcal{A}_1| \cdot |\Gamma_2|} \sum_{\alpha_1 \in \mathcal{A}_1} \int_{\Gamma_2} \mathcal{D}_{0\alpha_1}[H_1(b)] db.
\end{aligned}$$

Approximate by configuration sampling, domain truncation, and kernel polynomial approximation.

Electronic density of states for incommensurate layers. Daniel Massatt, Mitchell Luskin, and Christoph Ortner. SIAM J. Multiscale Modeling & Simulation, 15:476–499, 2017.

Twisted Bilayer Graphene Calculation

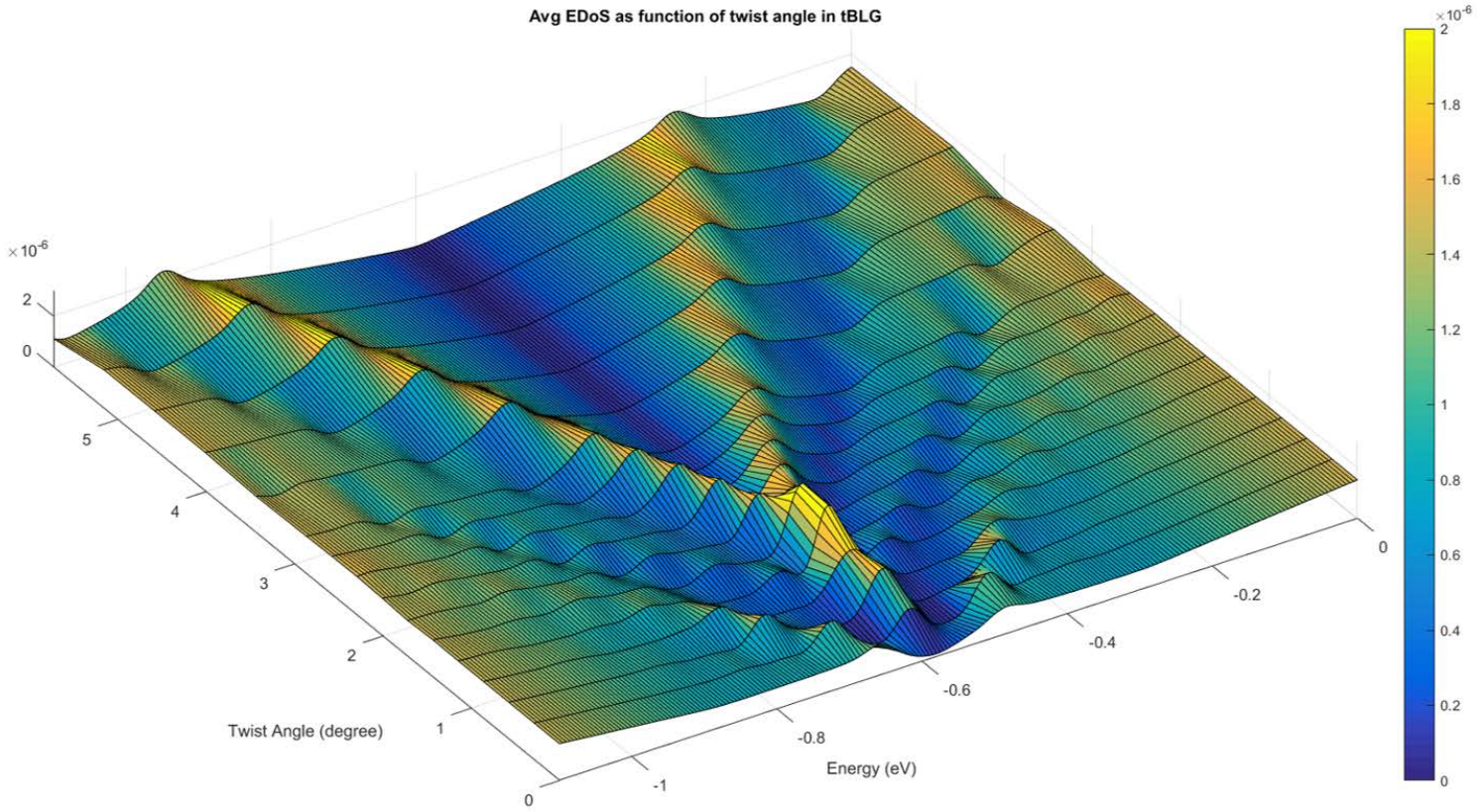

Figure: 500 Angstrom radius disk (600,000 atoms in total)

[Twistronics: manipulating the electronic properties of two-dimensional layered structures through the twist angle, Stephen Carr, Daniel Massatt, Shiang Fang, Paul Cazeaux, Mitchell Luskin, and Efthimios Kaxiras, Phys. Rev. B, 95:075420, 2017.]

Local Density of States in Twisted Bilayer Graphene

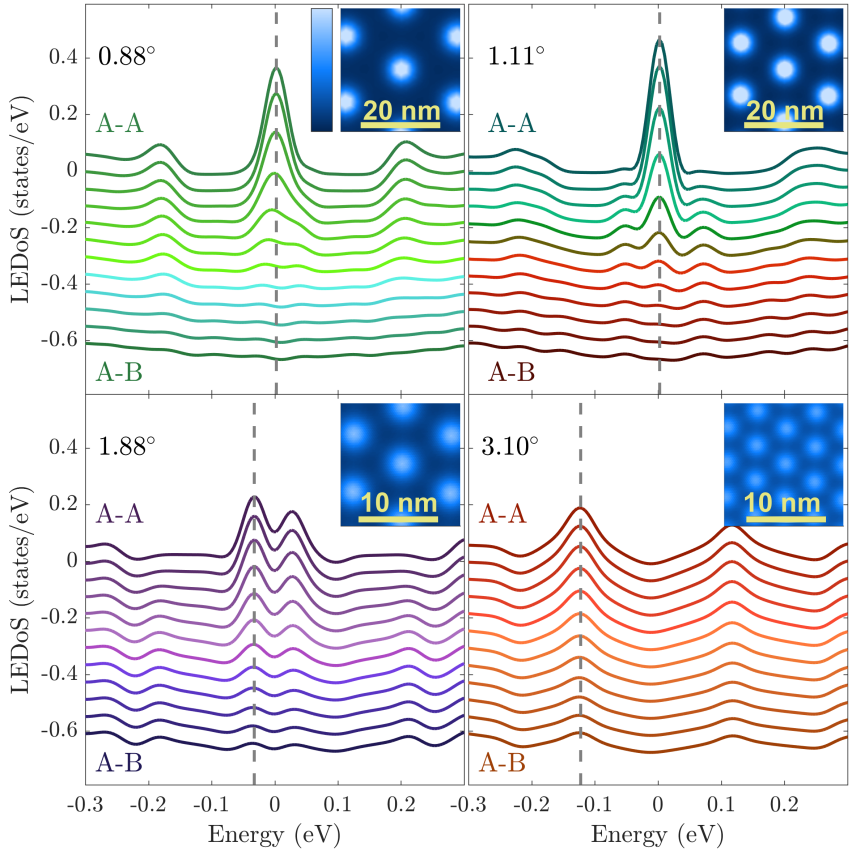

Figure: Simulated local electronic density of states (LEDoS) at four different angles of twisted bilayer graphene. Each line corresponds to a different real-space configuration along the line connecting AA to AB stacking. The insets show a real-space image of the density of states in the bilayer system at the energy value identified by a dashed line.

[Twistronics: manipulating the electronic properties of two-dimensional layered structures through the twist angle, Stephen Carr, Daniel Massatt, Shiang Fang, Paul Cazeaux, Mitchell Luskin, and Efthimios Kaxiras, Phys. Rev. B, 95:075420, 2017.]

Extensions to Band Structure, Transport, Relaxation

- Bloch transform incommensurate Hamiltonian to momentum space (not diagonal because of scattering between layers).
- Generalization of Kubo formula for optical conductivity to incommensurate structures by configuration-based current-current correlation measure

$$\mu = \nu\left(\int_{\Gamma_2} \mu_1[b]\, db + \int_{\Gamma_1} \mu_2[b]\, db\right), \qquad \text{and}$$

$$\sigma = -\int \frac{ie^2}{\hbar^2} \frac{f_\beta(E - E_F) - f_\beta(E' - E_F)}{(E - E')(E - E' + \omega + i\eta)}(E, E')\, d\mu(E, E').$$

- DoS, band structure and transport for relaxed incommensurate structures.

Generalized Kubo formulas for the transport properties of incommensurate 2D atomic heterostructures. E. Cancés, P. Cazeaux, and M. Luskin. Journal of Mathematical Physics, 58:063502, 2017.

Incommensurate heterostructures in momentum space. Daniel Massatt, Stephen Carr, Mitchell Luskin, and Christoph Ortner. Multiscale Model. Simul., 16:429–451, 2018.

Modeling and computation of Kubo conductivity for 2D incommensurate bilayers. Simon Etter, Daniel Massatt, Mitchell Luskin, and Christoph Ortner. Multiscale Model. Simul., 18:1525–1564, 2020.

Efficient computation of Kubo conductivity for incommensurate 2D heterostructures. D. Massatt, S. Carr, and M. Luskin. Eur. Phys. J. B, 93, 2020.

Electronic Observables for Relaxed Bilayer 2D Heterostructures in Momentum Space. Daniel Massatt, Stephen Carr, Mitchell Luskin, arXiv:2109.15296v3, 2021

Energy landscape in twisted bilayer graphene

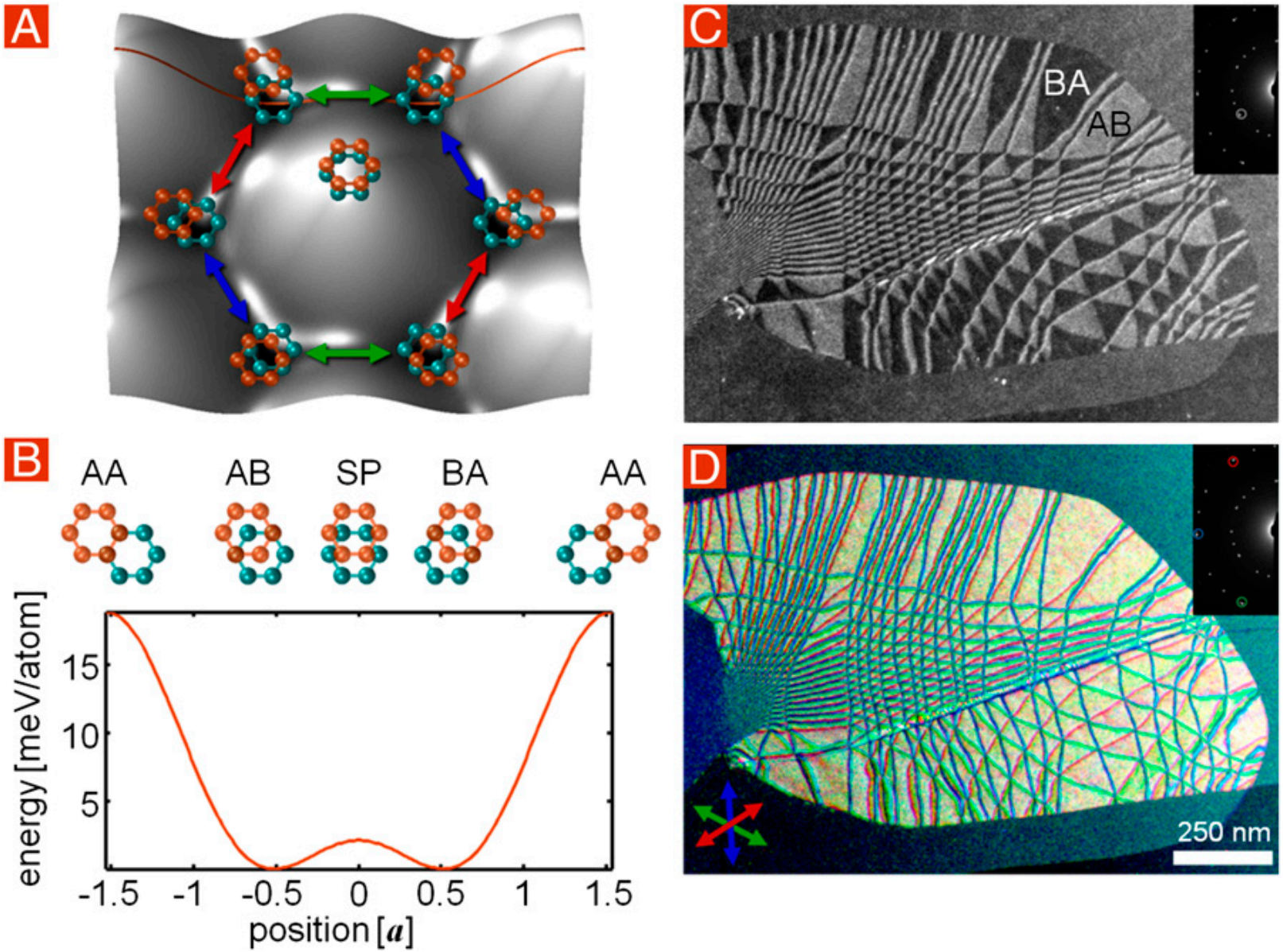

Strain solitons and topological defects in bilayer graphene. PNAS, 2013, Alden, . . . , McEuen

Continuum Model for Relaxation of Incommensurate 2D Bilayers

Approximate by a continuum model $E_{\text{tot}}(U_1, U_2)$ where $U_j(x) : \mathbb{R}^2 \to \mathbb{R}^2$ is the continuum displacement field for layer j :

$$E_{\text{tot}}(U_1, U_2) = \lim_{r\to\infty} \frac{1}{|B_r|} \int_{B_r} dx \big[\mathcal{E}^1_{\text{intra}}(\nabla U_1(x)) + \mathcal{E}^2_{\text{intra}}(\nabla U_2(x)) + \frac{1}{2}\mathcal{E}^1_{\text{inter}}(b_{1\to 2}(x) + U_1(x) - U_2(x)) + \frac{1}{2}\mathcal{E}^2_{\text{inter}}(b_{2\to 1}(x) + U_2(x) - U_1(x))\big]$$

where $\mathcal{E}^j_{\text{intra}}(\nabla U_j)$ is the intralayer elastic energy and

$$\mathcal{E}^1_{\text{inter}}(b_{1\to 2}(x) + U_1(x) - U_2(x))$$

is the relaxed Generalized Stacking Fault Energy, $\mathcal{E}^1_{\text{inter}} : \Gamma_2 \to \mathbb{R}$, where $b_{1\to 2}(x) \in \Gamma_2$ is the disregistry of layer 1 with respect to layer 2.

Disregistries $b_{1\to 2}(x)$ and $b_{2\to 1}(x)$ are periodic on moiré cell, $\Gamma_{\mathcal{M}}$.

Energy minimization of 2D incommensurate heterostructures. P. Cazeaux , M. Luskin, and D. Massatt. Arch. Rat. Mech. Anal., 235:1289–1325, 2019.

Generalized Stacking Fault Energy

The interlayer energy density of layer 2 with respect to layer 1 can be accurately modeled by the Generalized Stacking Fault Energy, F_{GSFE},

$$\mathcal{E}^2_{\text{inter}}(b_{2\to1}(x) + U_2(x) - U_1(x)) = F_{\text{GSFE}}(b_{2\to1}(x) + U_2(x) - U_1(x)),$$

where $b_{2\to1}(x)$ is the disregistry. F_{GSFE} can be fit by DFT.

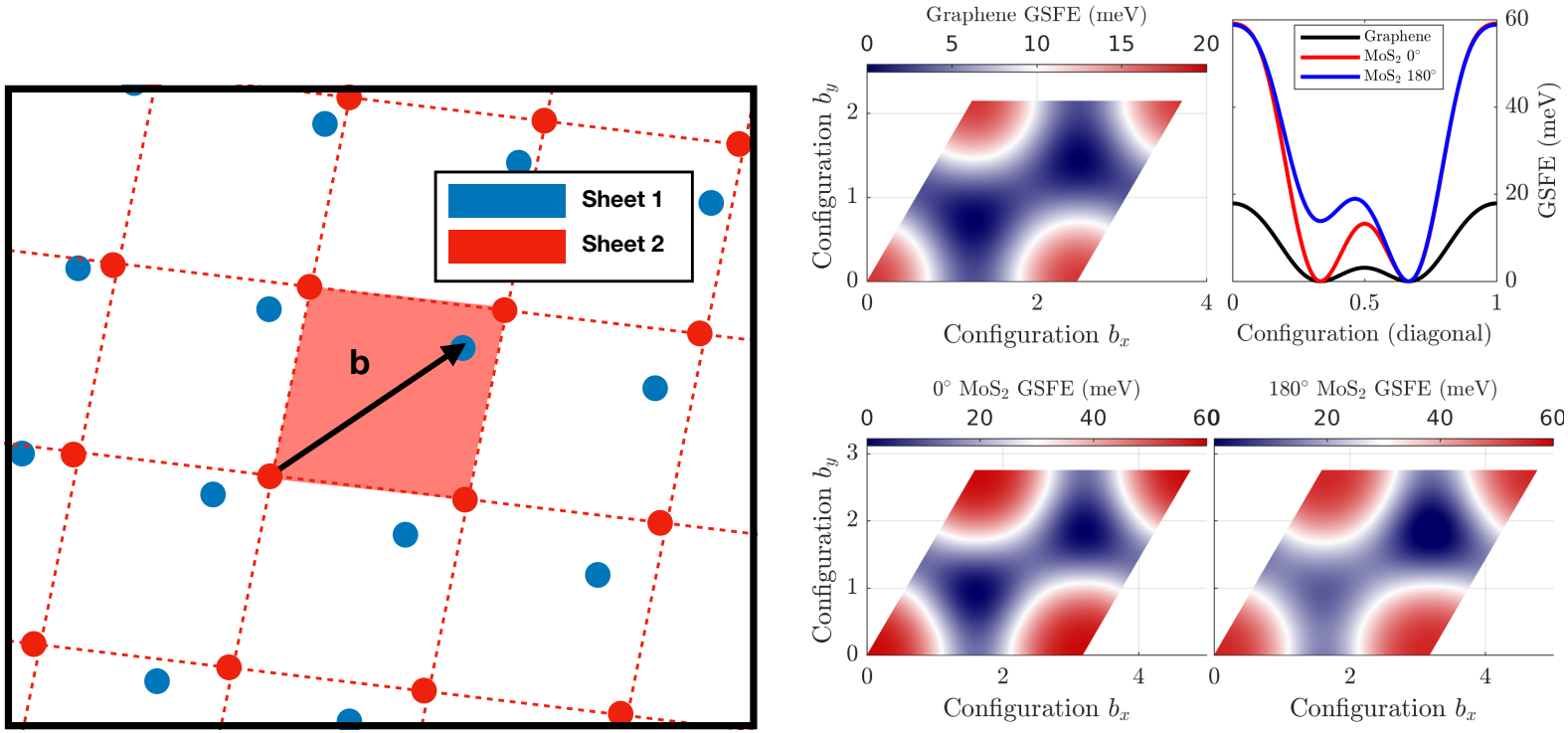

Figure: How the Generalized Stacking Fault Energy, which represents the interlayer coupling energy, depends on the disregistry b for three different materials.

Total Energy

The relation between displacement in configuration space coordinates and real space coordinates is given by

$$U_1(x) = u_1(b_{1\to 2}(x)) \quad \text{and} \quad U_2(x) = u_2(b_{2\to 1}(x)),$$

where u_1 is periodic on Γ_2 and u_2 is periodic on Γ_1. Since $b_{1\to 2}(x)$ and $b_{2\to 1}(x)$ are isomorphisms

$$b_{1\to 2} : \begin{cases} \Gamma_{\mathcal{M}} \to \Gamma_2, \\ \quad x \mapsto (I - A_2 A_1^{-1})x, \end{cases}$$

$$b_{2\to 1} : \begin{cases} \Gamma_{\mathcal{M}} \to \Gamma_1, \\ \quad x \mapsto (I - A_1 A_2^{-1})x, \end{cases}$$

we have that $U_1(x)$ and $U_2(x)$ are periodic on $\Gamma_{\mathcal{M}}$ and

$$\begin{aligned} &E_{\text{tot}}(U_1, U_2) \\ &= \int_{\Gamma_{\mathcal{M}}} dx \big[\mathcal{E}^1_{\text{intra}}(\nabla U_1(x)) + \mathcal{E}^2_{\text{intra}}(\nabla U_2(x)) \\ &\qquad + \frac{1}{2}\mathcal{E}^1_{\text{inter}}(b_{1\to 2}(x) + U_1(x) - U_2(x)) + \frac{1}{2}\mathcal{E}^2_{\text{inter}}(b_{2\to 1}(x) + U_2(x) - U_1(x)) \big]. \end{aligned}$$

Bilayer Graphene or MoS_2 Configuration Space Model

For bilayer graphene or MoS_2, $\mathcal{E}_{\text{intra}} = \mathcal{E}^1_{\text{intra}} = \mathcal{E}^2_{\text{intra}}$ since the intralayer energy is isotropic and

$$\mathcal{E}^1_{\text{inter}}(b_{1\to 2}(x)) = \mathcal{E}^2_{\text{inter}}(b_{2\to 1}(x))$$

by symmetry.

We can then obtain from the uniqueness of solutions to the energy minimization problem that $U_1 = -U_2$ and U_1 is the minimum displacement for the energy

$$E_{\text{tot}}(U) := \frac{1}{|\Gamma_M|}\int_{\Gamma_M} dx\big[\mathcal{E}_{\text{intra}}(\nabla U(x)) + \mathcal{E}^1_{\text{inter}}(b_{1\to 2}(x) + 2U(x))\big].$$

Rescale to Γ_0 to get Ginzburg-Landau type equation:

$$E_{\text{tot}}(U) := \int_{\Gamma_0} dx\big[\mathcal{E}_{\text{intra}}(\nabla U(x)) + \frac{1}{(2\sin\theta/2)^2}\mathcal{E}^1_{\text{inter}}(b_{1\to 2}(x) + 2U(x))\big].$$

Hence,

$$\int_{\Gamma_2} |\nabla u_1(b)|^2\, db \leqslant C\theta^{-2}, \quad \int_{\Gamma_{\mathcal{M}}} |\nabla U_1(x)|^2 dx \leqslant C\theta^{-2}.$$

Regularity of Displacement

$$\int_{\Gamma_2} |\nabla u_1(b)|^2 \, db \leqslant C\theta^{-2}, \qquad \int_{\Gamma_{\mathcal{M}}} |\nabla U_1(x)|^2 dx \leqslant C\theta^{-2}.$$

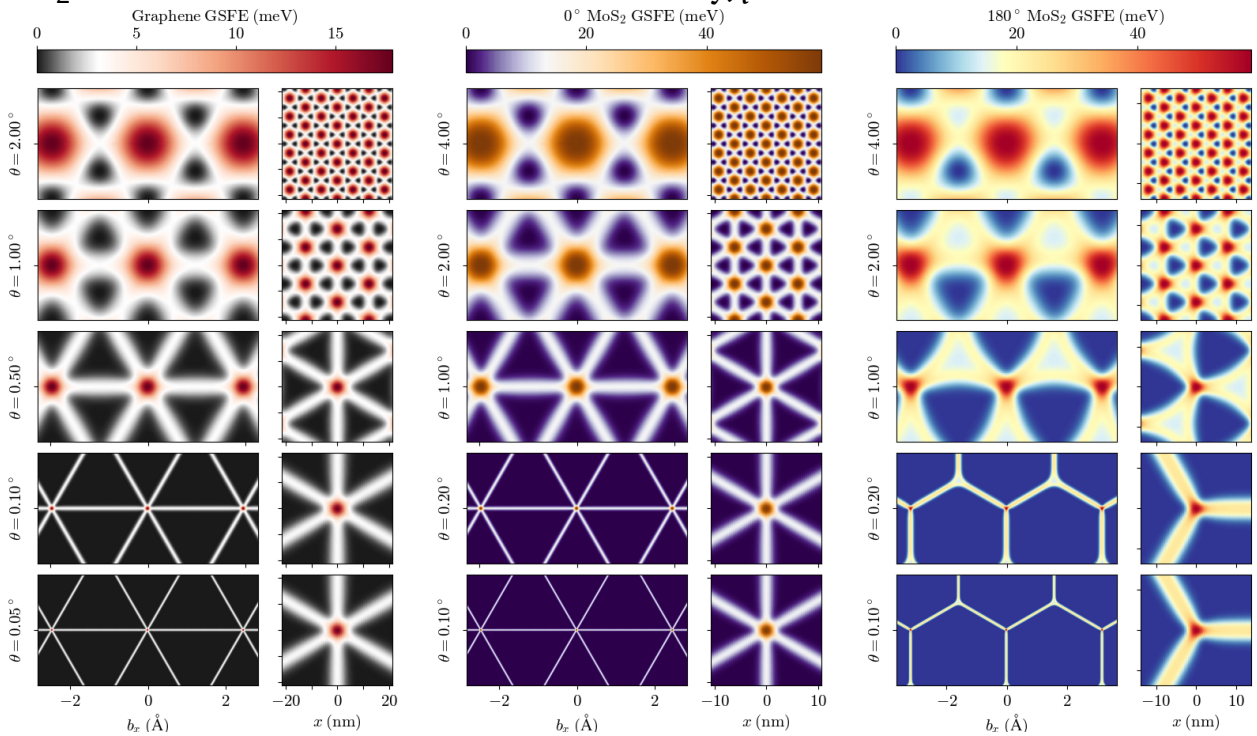

Figure: Relaxation results for twisted bilayers with five incommensurate twist angles each. The left panel of each column shows $F_{\mathrm{GSFE}}(\mathbf{b} + 2\mathbf{u}(\mathbf{b}))$ over Γ (the relaxation pattern in configuration space) and the right panel shows $F_{\mathrm{GSFE}}(\mathbf{r})$ (over real space).

Relaxation and Domain Formation in Incommensurate 2D Heterostructures. S. Carr, D. Massatt, S. B. Torrisi, P. Cazeaux, M. Luskin and E. Kaxiras). Physical Review B, page 224102 (7 pp), 2018.

Relaxation and domain wall structure of bilayer moiré systems. Paul Cazeaux, Drake Clark, Rebecca Engelke, Philip Kim, and Mitchell Luskin. Journal of Elasticity, to appear.

Diffraction Patterns with Tunable Commensurability

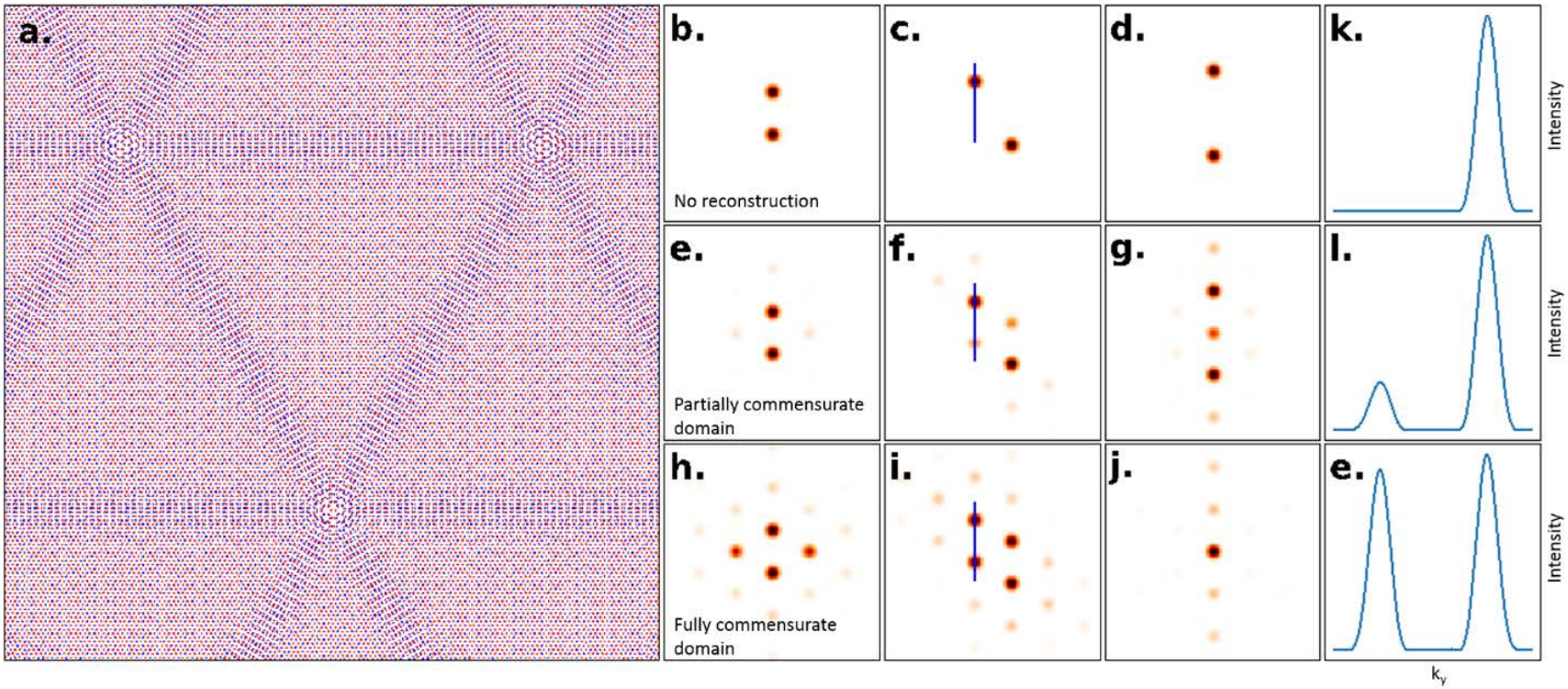

Figure: Reconstructed lattice structures and their simulated diffraction patterns with tunable commensurability. a, Modeled lattice structure with fully commensurate domains. b, c, d, Diffraction peaks appearing around g=$10\bar{1}0, 11\bar{2}0, 20\bar{2}0$ Bragg peaks without any reconstruction. Line cut of the diffraction peak intensity along the line in c, f, i.

[*Atomic and electronic reconstruction at van der Waals interface in twisted bilayer graphene* , Hyobin Yoo, Rebecca Engelke, Stephen Carr, Shiang Fang, Kuan Zhang, Paul Cazeaux, Suk Hyun Sung, Robert Hovden, Adam W. Tsen, Takashi Taniguchi, Kenji Watanabe, Gyu-Chul Yi, Miyoung Kim, Mitchell Luskin, Ellad B. Tadmor, Efthimios Kaxiras, Philip Kim, *Nature Materials*, 2019]

Vortices and Anti-Vortices

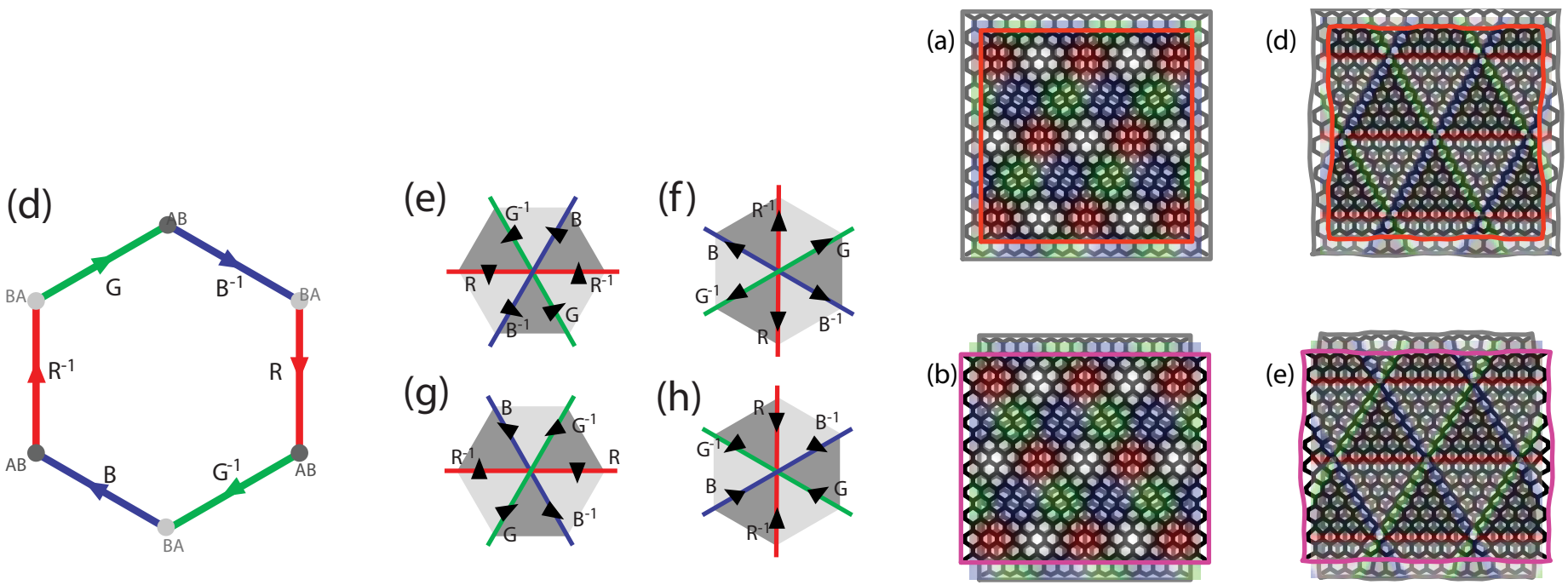

Figure: Left: (d) Clockwise (vortex) or counterclockwise paths (anti-vortex) around an AA point determine the order of R, G and B elements. Real space arrangement of dislocations: corresponding to clockwise (e isotropic, f twist) and counterclockwise (g pure shear, h simple shear) paths in configuration space. Right: moiré from (a) isotropic scaling and (b) pure shear. Relaxed moiré from (d) isotropic scaling and (e) pure shear.

Topological nature of dislocation networks in two-dimensional moir´e materials. R. Engelke, H. Yoo, S. Carr, M. Luskin, E. Kaxiras,. . . , P. Kim. Phys. Rev. B, 107:125413, 2023.

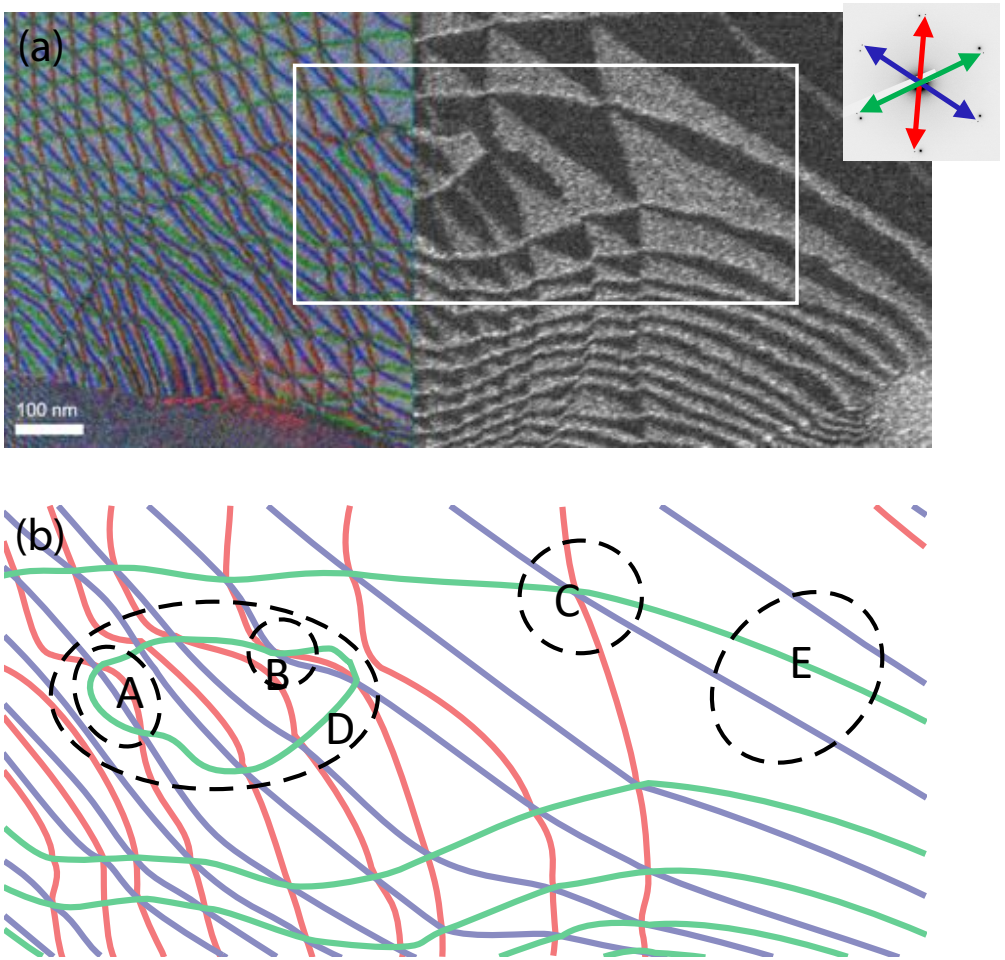

Figure: a) Dark field image of twisted bilayer graphene containing antivortices along a bubble edge. b) Loops are drawn and topological number of each loop is counted. A) Vortex-antivortex pair, $w = 0$. B) Antivortex, $w = -1$. C) Vortex, $w = +1$. D) Closed-loop dislocation, $w = 0$. E) Linear domains, $w = 0$.

Topological nature of dislocation networks in two-dimensional moir´e materials. R. Engelke, H. Yoo, S. Carr, M. Luskin, E. Kaxiras,. . . , P. Kim. Phys. Rev. B, 107:125413, 2023.

Twisted Trilayer Honeycomb Lattice

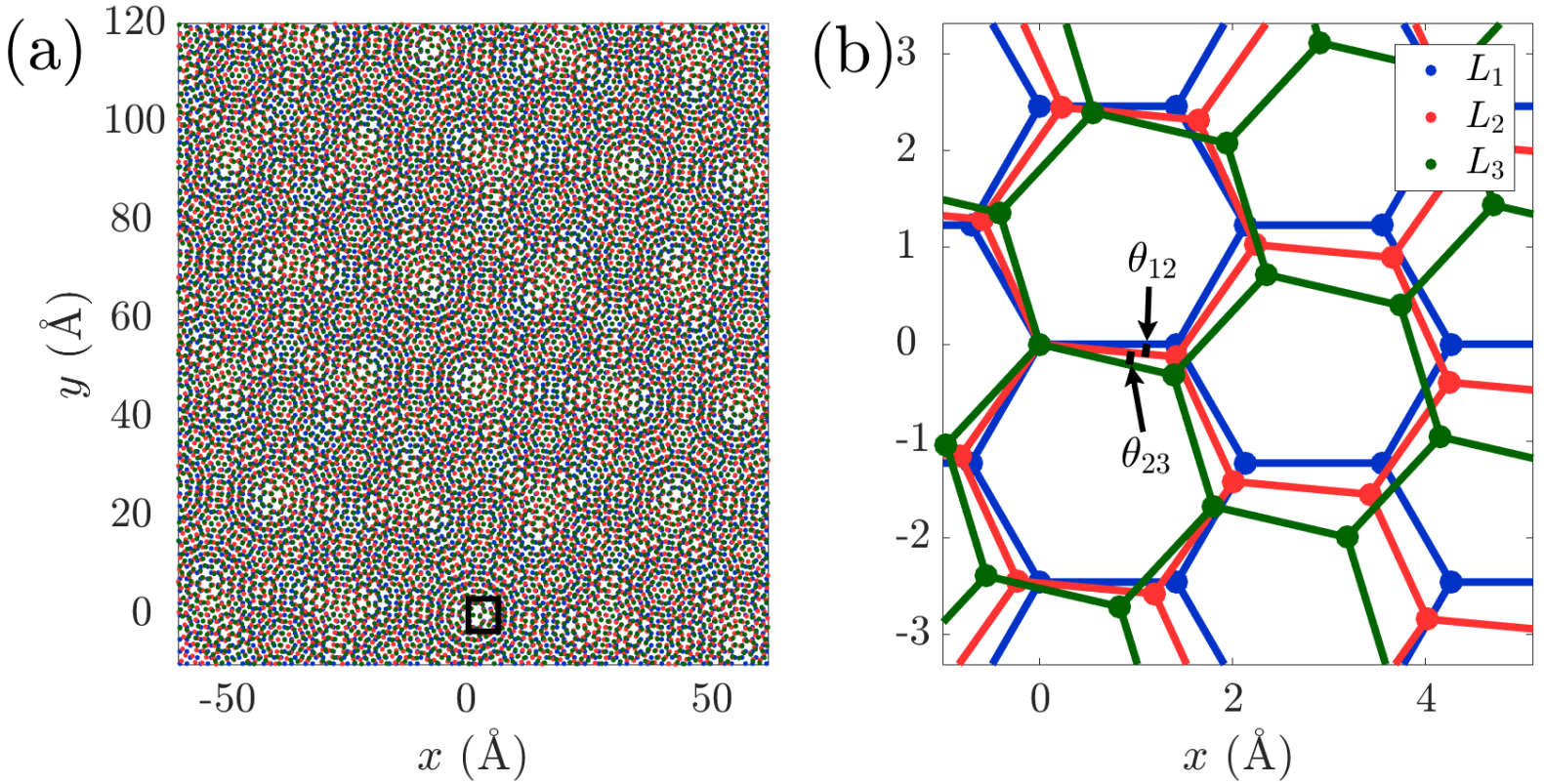

Figure: (a) An example of a twisted trilayer honeycomb lattice in real space with $\theta_{12} = 5.3^\circ$ and $\theta_{23} = 7.7^\circ$. (b) Magnified view at the black box marked in (a). The twist angle between L_1 and L_2, θ_{12}, and the twist angle between L_2 and L_3, θ_{23}, are marked by black arrows.

Twisted Trilayer Configuration Space

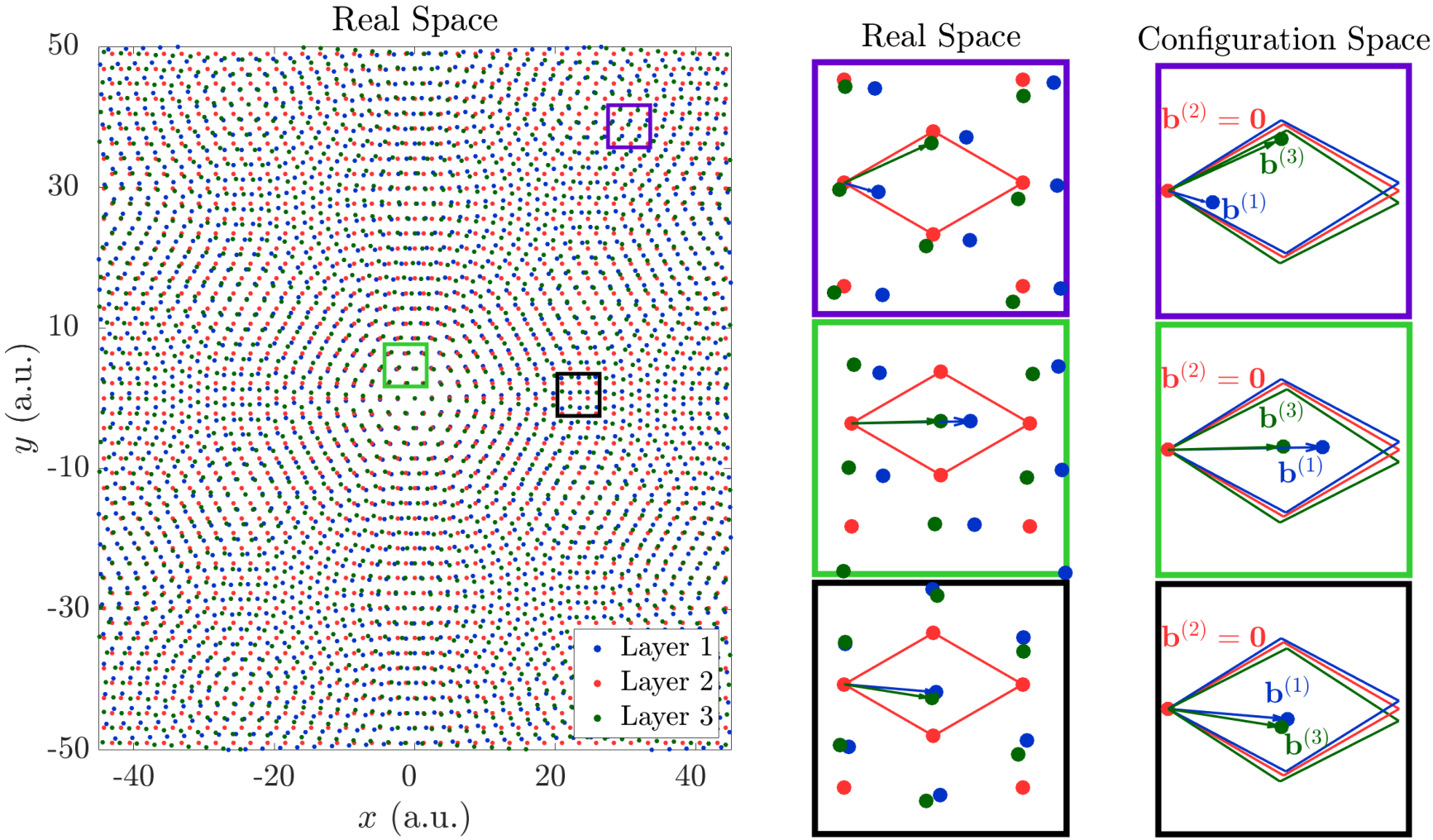

Figure: The first layer (blue) is twisted by 2° with respect to the second layer (red), and the third layer (green) is twisted by 3° with respect to the second.
The configuration space $X_2 := \Gamma_1 \times \Gamma_3$ is uniformly sampled.

Moire patterns as beating phenomena

Consider the oscillations of layer ℓ given by $h_\ell(r) = \sum_{k=1}^{2} A_{\ell,k} e^{ib_{\ell,k}\cdot r}$. Then

$$\begin{aligned} h_M(r) &= h_1(r) + h_2(r) \\ &= \sum_{k=1}^{2} A_{1,k} e^{i\left(\frac{b_{1,k}+b_{2,k}}{2}\right)\cdot r} e^{i\left(\frac{b_{1,k}-b_{2,k}}{2}\right)\cdot r} + A_{2,k} e^{i\left(\frac{b_{1,k}+b_{2,k}}{2}\right)\cdot r} e^{-i\left(\frac{b_{1,k}-b_{2,k}}{2}\right)\cdot r}. \end{aligned}$$

Fast oscillations with wave number $\left(\frac{b_{1,k}+b_{2,k}}{2}\right)$.

Slow beating oscillations with wave number $\left(\frac{b_{1,k}-b_{2,k}}{2}\right)$.

$(m_1,\ m_2)$ harmonic. Now $h_\ell(r) = \sum_{k=1}^{2} A_{\ell,k} e^{im_\ell b_{\ell,k}\cdot r}$. Then

$$\begin{aligned} h_M(r) &= h_1(r) + h_2(r) \\ &= \sum_{k=1}^{2} A_{1,k} e^{i\left(\frac{m_1 b_{1,k}+m_2 b_{2,k}}{2}\right)\cdot r} e^{i\left(\frac{m_1 b_{1,k}-m_2 b_{2,k}}{2}\right)\cdot r} + A_{2,k} e^{i\left(\frac{m_1 b_{1,k}+m_2 b_{2,k}}{2}\right)\cdot r} e^{-i\left(\frac{m_1 b_{1,k}-m_2 b_{2,k}}{2}\right)\cdot r}. \end{aligned}$$

Fast oscillations with wave number $\left(\frac{m_1 b_{1,k}+m_2 b_{2,k}}{2}\right)$.

Slow beating oscillations with wave number $\left(\frac{m_1 b_{1,k}-m_2 b_{2,k}}{2}\right)$.

Moiré of moiré superlattice

Reciprocal moiré lattice vectors for layers i and j are given by columns of

$$\mathcal{R}^*_{\mathcal{M}_{ij}} = 2\pi(A_i^{-T} - A_j^{-T})\mathbb{Z}^2 := G_{ij}\mathbb{Z}^2.$$

The (m, n) harmonic for TTG is given by the reciprocal superlattice

$$\mathcal{R}^*_{m,n} = (mG_{12} - nG_{23})\mathbb{Z}^2.$$

and corresponding superlattice

$$\mathcal{R}_{m,n} = (2\pi)^{-1}(mG_{12} - nG_{23})^{-T}\mathbb{Z}^2.$$

The length of (m, n) harmonic, $\|(mG_{12} - nG_{23})^{-T}\|$, is not necessarily the largest for the $(1, 1)$ mode.

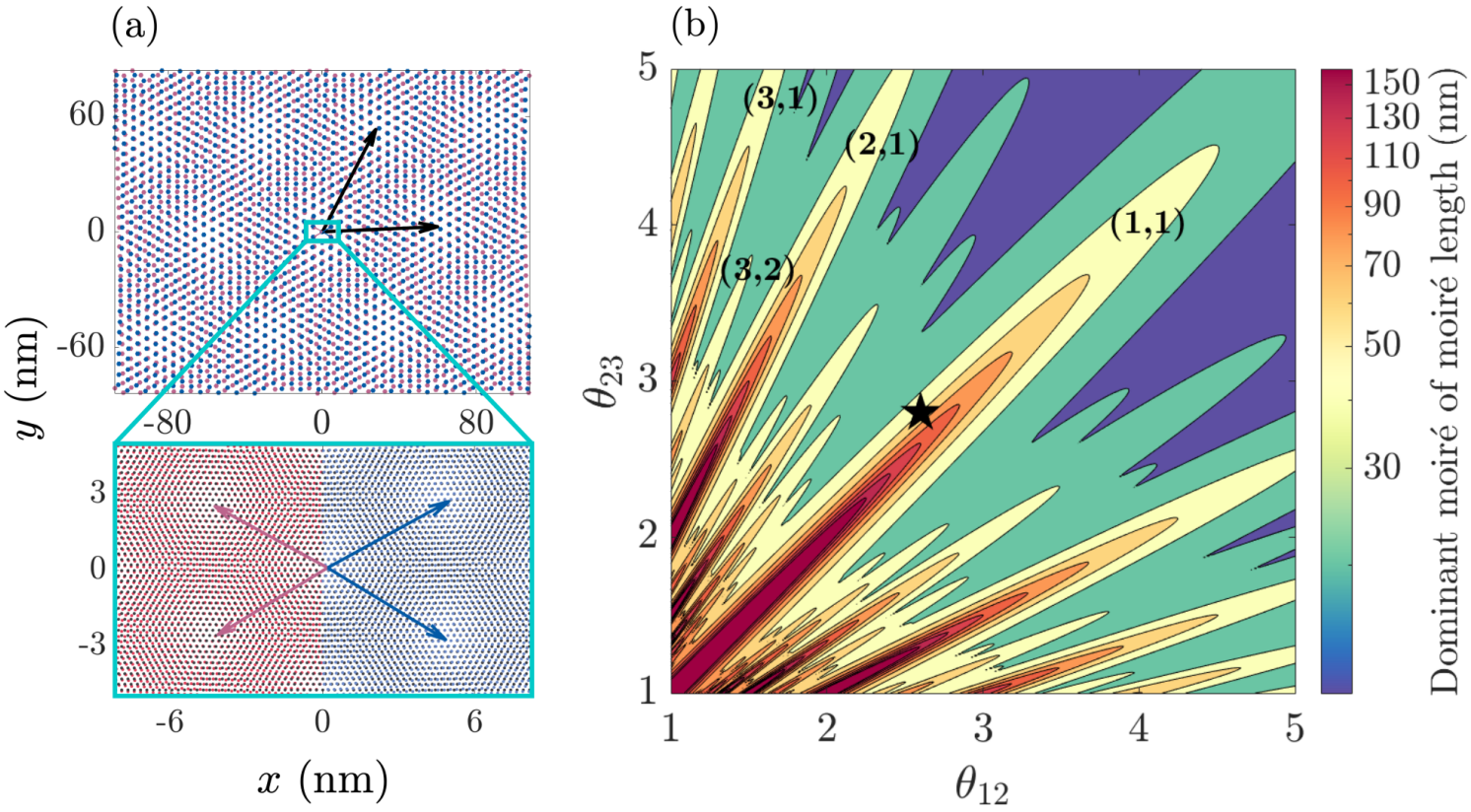

Figure: Illustration of moiré of moiré pattern in tTLG for $\theta_{12} = 2.6^\circ$, $\theta_{23} = 2.8^\circ$. Red and blue points represent the lattice points of the bilayer moiré supercells between L1–L2 and L2–L3 respectively. (b) The dominant moiré of moiré length scale on a logarithmic color scale. The black star corresponds to the twist angle in (a), and (m, n) labels the moiré of moiré harmonic that the nearby lobe corresponds to.

Energy minimization of 2D incommensurate heterostructures. P. Cazeaux , M. Luskin, and D. Massatt. Arch. Rat. Mech. Anal., 235:1289–1325, 2019.

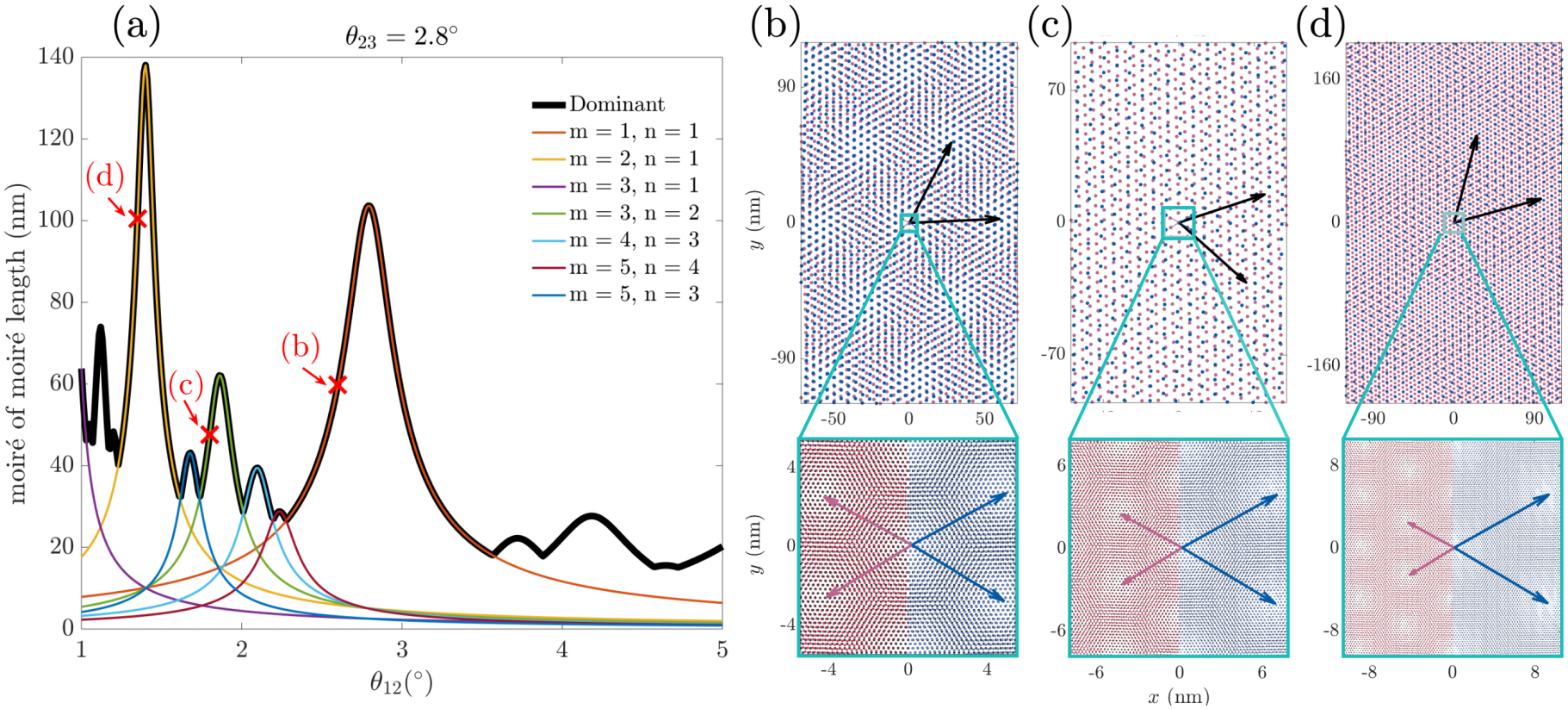

Figure: (a) Moiré of moiré of lengths $\lambda^{\mathrm{H}}_{mn}$ as a function of θ_{12} for $\theta_{23} = 2.8^{\circ}$. The thick black line indicates the dominant length. (b)-(d) Example moiré of moiré geometries, corresponding to the red crosses in (a). Top: red and blue scattered points are the lattice points of the bilayer moiré supercells between L1, L2 and L2, L3 respectively. Black vectors indicate estimated dominant moiré of moiré supercell lattice vectors. A blow-up of the small boxed area is shown below, with points representing the atomic positions of each monolayer graphene, for L1 and L2 on the left half and for L2 and L3 on the right half. Red and blue vectors are the bilayer moiré lattice vectors of L1, L2 and L2, L3 respectively.

Relaxation of Tristed Trilayer Heterostructures

For twisted trilayer heterostructures, the configuration is not periodic on any two-dimensional domain, so we have to consider the large body limit

$$E_{\mathrm{tot}}(U_1, U_2, U_3) = \lim_{r\to\infty} \frac{1}{|B_r|} \int_{B_r} dx \Bigg[\sum_{j=1}^{3} \mathcal{E}^j_{\mathrm{intra}}(\nabla U_j(x)) + \frac{1}{2} \sum_{j=1}^{2} \mathcal{E}^{j+}_{\mathrm{inter}}(b_{j\to j+1}(x) + U_j(x) - U_{j+1}(x)) + \frac{1}{2} \sum_{j=2}^{3} \mathcal{E}^{j-}_{\mathrm{inter}}(b_{j\to j-1}(x) + U_j(x) - U_{j-1}(x)) \Bigg]$$

where $\mathcal{E}^j_{\mathrm{intra}}(\nabla U_j(x))$ is the intralayer elastic energy, $\mathcal{E}^{j\pm}_{\mathrm{inter}}(b) : \Gamma_{j\pm1} \to \mathbb{R}$ is the interlayer generalized stacking fault energy of layer j with respect to layer $j \pm 1$, and $b_{j\to j\pm1}(x)$ is the reference local disregistry of layer j with respect to layer $j \pm 1$.

Note that $b_{j\to j+1}(x)$ and $b_{j+1\to j}(x)$ are periodic on the moiré cell $\Gamma^{jj+1}_{\mathcal{M}}$, and the moiré cells $\Gamma^{jj+1}_{\mathcal{M}}$ are incommensurate.

Relaxation of Incommensurate Twisted Trilayer Graphene

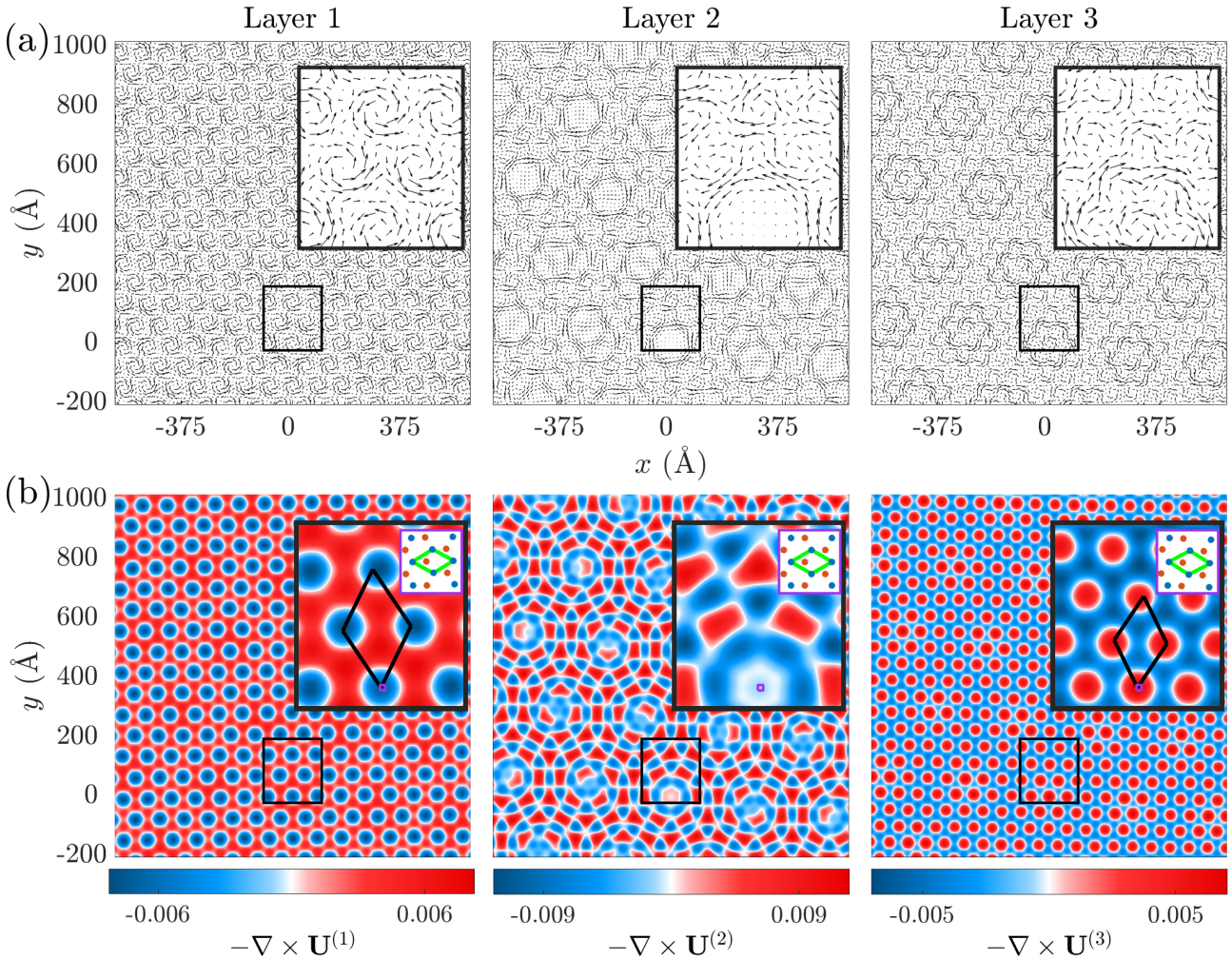

Figure: Real space relaxation pattern for twisted trilayer graphene with $\theta_{12} = 1.73^\circ$, $\theta_{23} = 2.24^\circ$, using discretization $N = 81$.

[*Modeling mechanical relaxation in incommensurate trilayer van der Waals heterostructures*, Ziyan Zhu, Paul Cazeaux, Mitchell Luskin, and Efthimios Kaxiras, *Physical Review B,*, 2020]

Configuration-based Intralayer Energy

Define the displacement in configuration space $\mathbf{u}_j(b_{j\to 1}, \ldots, b_{j\to j-1}, b_{j\to j+1}, \ldots, \ldots, b_{j\to 3})$ by

$$U_j(x) := \mathbf{u}_j(b_{j\to 1}(x), \ldots, b_{j\to j-1}(x), b_{j\to j+1}(x), \ldots, \ldots, b_{j\to 3}(x)).$$

The spatial gradient of the atomistic displacement is

$$\nabla U_j(x) = \sum_{i\neq j} \nabla_{b_{j\to i}} \mathbf{u}_j \cdot (\mathrm{I} - A_i A_j^{-1}) =: \hat{\nabla}_{\mathbf{x}} \mathbf{u}_j(b_{j\to i}).$$

We can then model the intralayer energy by the Cauchy-Born approximation or even linear elasticity

$$E_{\mathrm{intra}}(\mathbf{u}) := \sum_{j=1}^{3} \fint_{X_j} \mathcal{E}^j_{\mathrm{intra}}(\hat{\nabla}_{\mathbf{x}} \mathbf{u}_j)\, db_{j\to 1} \ldots db_{j\to p},$$

where $X_j = \times_{i\neq j} \Gamma_i$.

$\hat{\nabla}_{\mathbf{x}} \mathbf{u}_j(b_{j\to i})$ is a directional derivative for a 2-dimensional submanifold of the 4-dimensional torus X_j, so the Euler-Lagrange PDE is nonelliptic.

Incommensurability gives a small divisor problem for a hypoelliptic operator.

Fourier Analysis of Intralayer Energy

Let $G^{(j)} \in \mathcal{R}_j^*$ and let the Fourier coefficients $\tilde{\mathbf{u}}^{(i)}$ be defined according to

$$\mathbf{u}^{(i)}(b_{i\to j}, b_{i\to k}) = \sum_{G^{(j)},\, G^{(k)}} \tilde{\mathbf{u}}^{(i)}(G^{(j)},\, G^{(k)}) \times \exp\{i(G^{(j)} \cdot b_{i\to j} + G^{(k)} \cdot b_{i\to k})\}.$$

The contribution of the mode $(G^{(j)}, G^{(k)})$ to the variational elastic energy is

$$\mathcal{E}^i_{\text{intra}}(G^{(j)}, G^{(k)}) = \frac{1}{2}\left[\tilde{u}^{(i)}(G^{(j)}, G^{(k)}) \otimes \left(M_{ji}^T G^{(j)} + M_{jk}^T G^{(k)}\right)\right] : C :$$
$$\left[\tilde{u}^{(i)}(G^{(j)}, G^{(k)}) \otimes \left(M_{ji}^T G^{(j)} + M_{jk}^T G^{(k)}\right)\right]$$

where $M_{ji} = I - A_j A_i^{-1}$ and C is the isotropic linear elastic strain rank 4 tensor

$$C_{11ij} = \begin{pmatrix} K+G & 0 \\ 0 & G \end{pmatrix} \quad C_{12ij} = \begin{pmatrix} 0 & K-G \\ G & 0 \end{pmatrix}$$
$$C_{21ij} = \begin{pmatrix} 0 & G \\ K-G & 0 \end{pmatrix} \quad C_{22ij} = \begin{pmatrix} G & 0 \\ 0 & K+G \end{pmatrix}.$$

Nonsingularity of Euler-Lagrange PDE

The Euler-Lagrange PDE is nonetheless nonsingular since

$$\mathcal{E}_1(G^{(2)}, G^{(3)}) = 0 \text{ if and only if } \tilde{u}_1(G^{(2)}, G^{(3)}) = 0 \text{ or } G^{(2)} = G^{(3)} = 0$$

and similarly for $\mathcal{E}_2(G^{(1)}, G^{(3)})$ and $\mathcal{E}_3(G^{(1)}, G^{(2)})$.

To see this, note that $\mathcal{E}_1(G^{(2)}, G^{(3)}) \propto |M_{21}^T G^{(2)} + M_{31}^T G^{(3)}|^2$ and

$$M_{21}^T G^{(2)} + M_{31}^T G^{(3)} = -G'^{(1)} + G^{(2)} + G^{(3)},$$

where $G'^{(1)} = A_1^{-T} A_2^T G^{(2)} + A_1^{-T} A_3^T G^{(3)} \in \mathcal{R}_1^*$ and

$$-G'^{(1)} + G^{(2)} + G^{(3)} = 0 \text{ if and only if } G'^{(1)} = G^{(2)} = G^{(3)} = 0$$

by the incommensurability assumption of the trilayer.

Observe that $|G'^{(1)} - G^{(2)} - G^{(3)}|^2$ and hence $\mathcal{E}_1(G^{(2)}, G^{(3)})$ can be small even though $G^{(2)}$ and $G^{(3)}$ are large, which is contrary to the ellipticity condition that $\mathcal{E}_1(G^{(2)}, G^{(3)})$ is a uniformly positive definite quadratic form in $(G^{(2)}, G^{(3)})$ for all Fourier coefficients $\tilde{u}^{(1)}(G^{(2)}, G^{(3)})$ of the displacement.

Configuration-based Interlayer Energy

Similarly, the interlayer misfit energy can be modeled by

$$E_{\text{inter}}(\mathbf{u}) = \frac{1}{2}\sum_{j=1}^{p-1} \fint_{X_j} \mathcal{E}^{j+}_{\text{inter}}(\hat{\mathbf{B}}_{j\to j+1}(\omega)) + \frac{1}{2}\sum_{j=2}^{p} \fint_{X_j} \mathcal{E}^{j-}_{\text{inter}}(\hat{\mathbf{B}}_{j\to j-1}(\omega))$$

where $\hat{\mathbf{B}}_{j\to j\pm1}(b_{j\to i})$ is the interpolated modulated local disregistry :

$$\Gamma_{j\pm1} \ni \hat{\mathbf{B}}_{j\to j\pm1}(b_{j\to i}) = b_{j\to j\pm1} + \mathbf{u}_{j\pm1}\left(b_{j\to i} - A_i A_{j\pm1}^{-1} b_{j\to j\pm1}\right) - \mathbf{u}_j(b_{j\to i})$$

since

$$b_{j\pm1\to i}(x) = b_{j\to i}(x) - A_i A_{j\pm1}^{-1} b_{j\to j\pm1}(x).$$

Finally, we formulate the mechanical relaxation of the multilayers by

$$\mathbf{u}^{\text{c}} \in \arg\min\left\{ E_{intra}(\mathbf{u}) + E_{\text{inter}}(\mathbf{u}) \quad | \quad \mathbf{u}_j \in H^1 \cap W^{1,\infty}(X_j;\mathbb{R}^2) \right\}.$$

Energy minimization of 2D incommensurate heterostructures. P. Cazeaux , M. Luskin, and D. Massatt. Arch. Rat. Mech. Anal., 235:1289–1325, 2019.

Transform to Momentum Space

For the wave function $\psi := (\psi_1, \ldots, \psi_p)$,

$$(H_{jj}\psi_j)(R_j) = \sum_{R_j' \in \mathcal{R}_j} h_{jj}(R_j - R_j')\psi_j(R_j'), \quad R_j,\, R_j' \in \mathcal{R}_j,$$

$$(H_{jk}\psi_k)(R_j) = \sum_{R_k \in \mathcal{R}_k} h_{jk}(R_j - R_k)\psi_k(R_k), \quad R_j, \in \mathcal{R}_j\, R_k, \in \mathcal{R}_k.$$

Define the Bloch transform for each sheet

$$\breve{\psi}_j(q) = |\Gamma_j^*|^{-1/2} \sum_{R_j \in \mathcal{R}_j} \psi_{R_j} e^{-iR_j \cdot q}, \qquad q \in \Gamma_j^*.$$

Transform the Hamiltonian to momentum space

$$\widetilde{H_{jj}\psi_j}(q) = c_j \widetilde{h_{jj}}(q)\breve{\psi}_j(q), \qquad q \in \Gamma_j^*,$$

$$\widetilde{H_{jk}\psi_k}(q) = \sum_{G_j \in \mathcal{R}_j^*} c_{jk}\widehat{h_{jk}}(q + G_j)\widetilde{\psi_k}(q + G_j), \qquad j \neq k,\ q \in \Gamma_j^*,$$

where $c_j = |\Gamma_j^*|^{1/2}$, $c_{jk} = c_j \cdot c_k$, and

$$\widetilde{h_{jj}}(q) = |\Gamma_j^*|^{-1/2} \sum_{R_j \in \mathcal{R}_j} h_{jj}(R_j) e^{-iR_j \cdot q}, \qquad q \in \Gamma_j^*,$$

$$\widehat{h_{jk}}(q) = \frac{1}{2\pi} \int h_{jk}(x) e^{-ix \cdot q} dx, \qquad j \neq k,\ q \in \mathbb{R}^2.$$

Interlayer Scattering

Transform the Hamiltonian to momentum space

$$\widetilde{H_{jj}\psi_j}(q) = c_j \widetilde{h_{jj}}(q)\check{\psi}_j(q), \qquad q \in \mathrm{BZ}_j,$$
$$\widetilde{H_{jk}\psi_k}(q) = \sum_{G_j \in \mathcal{R}_j^*} c_{jk}\widehat{h_{jk}}(q+G_j)\widetilde{\psi_k}(q+G_j), \qquad j \neq k,\ q \in \mathrm{BZ}_j.$$

We thus see that

$$\check{\psi}_j(q) \text{ scatters to } \widetilde{\psi_k}(q+G_j) = \widetilde{\psi_k}(q+G_j-G_k), \quad G_j \in \mathcal{R}_j,\ G_k \in \mathcal{R}_k.$$

No periodicity if lattices are incommensurate!

Bilayer:

$$\widetilde{\psi_1}(q) \text{ scatters to } \widetilde{\psi_2}(q+G_1-G_2), \quad G_1 \in \mathcal{R}_1,\ G_2 \in \mathcal{R}_2.$$
$$\widetilde{\psi_2}(q+G_1-G_2) \text{ scatters to } \widetilde{\psi_1}(q+(G_1-G_2)+(G_2'-G_1'))$$
$$= \widetilde{\psi_1}(q+(G_1-G_1')-(G_2-G_2')), \quad G_2' \in \mathcal{R}_2,\ G_1' \in \mathcal{R}_1.$$

Low energy continuum approximation gives periodicity in bilayer, not for $p > 2$

Electronic band structure: unrelaxed vs. relaxed

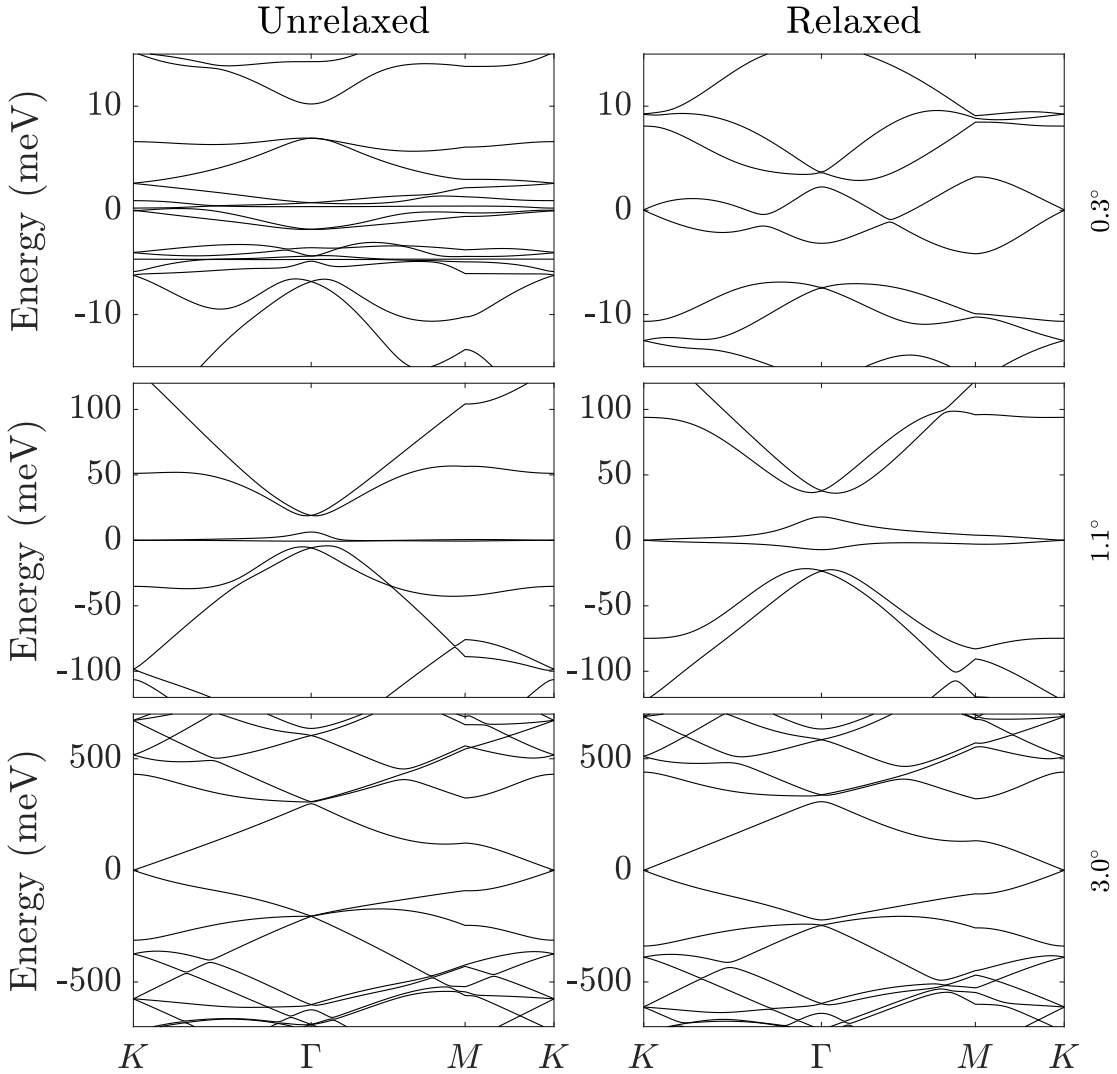

Figure: Electronic band structure along high-symmetry lines of the moiré Brillouin zone at a single monolayer K valley for 0.3° (top), 1.1° (middle), and 3.0° (bottom).

Electronic Observables for Relaxed Bilayer 2D Heterostructures in Momentum Space, Daniel Massatt, Stephen Carr, Mitchell Luskin, arXiv:2109.15296v3, 2021

Interlayer hopping functions for unrelaxed and relaxed 2D bilayers

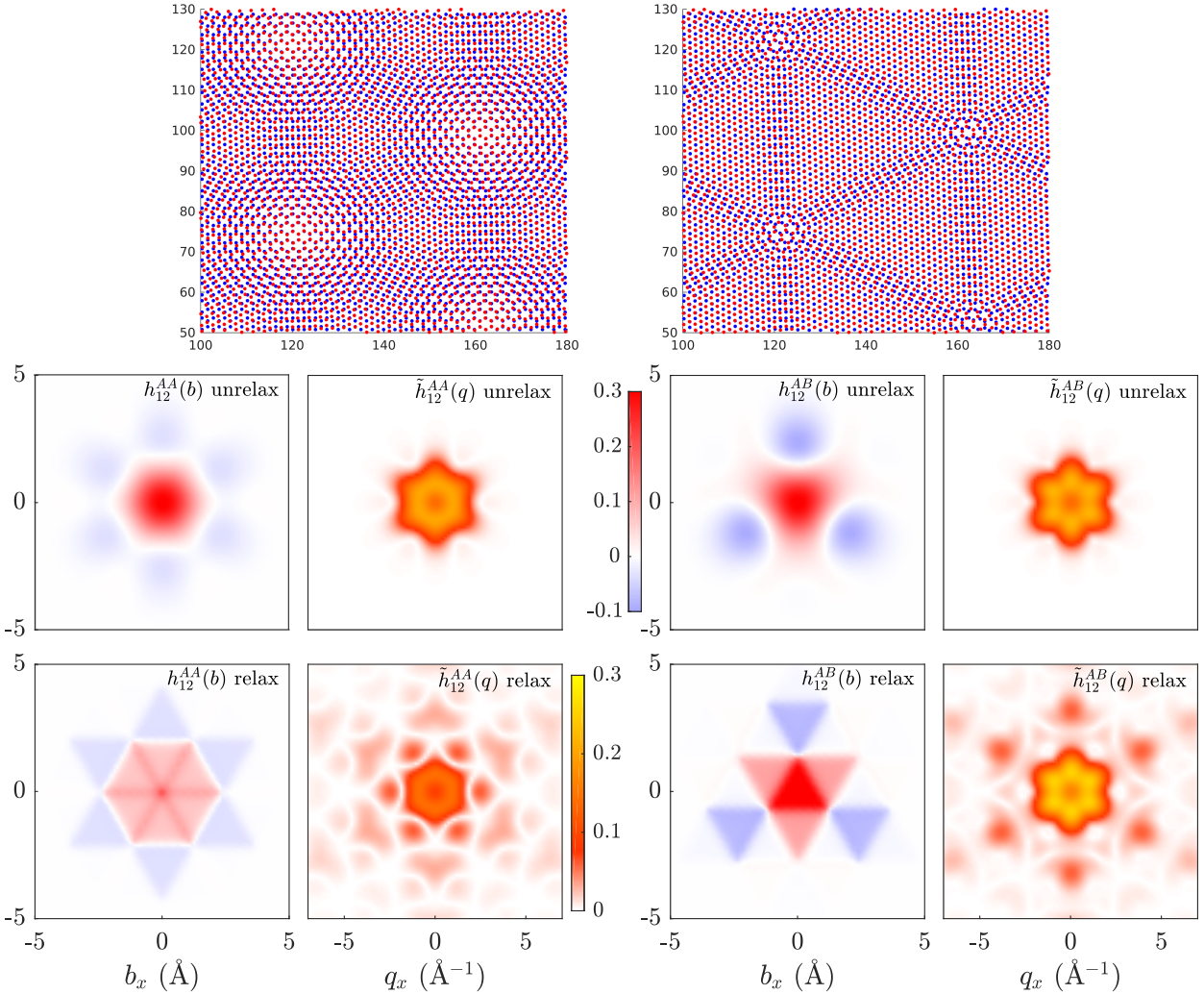

Figure: Interlayer coupling for small twist angle $\theta = 0.3^\circ$ in real and momentum space. Real space methods suffer a loss of regularity with respect to configuration, while momentum space suffers with slower reciprocal space localization.

Electronic Observables for Relaxed Bilayer 2D Heterostructures in Momentum Space, Daniel Massatt, Stephen Carr, Mitchell Luskin, arXiv:2109.15296v3, 2021

Degrees of Freedom Comparison Between TBLG & TTLG

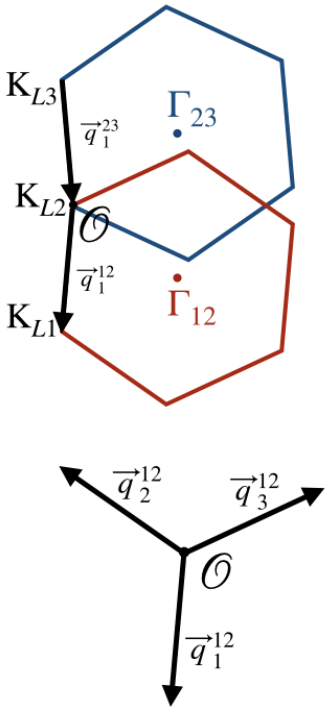

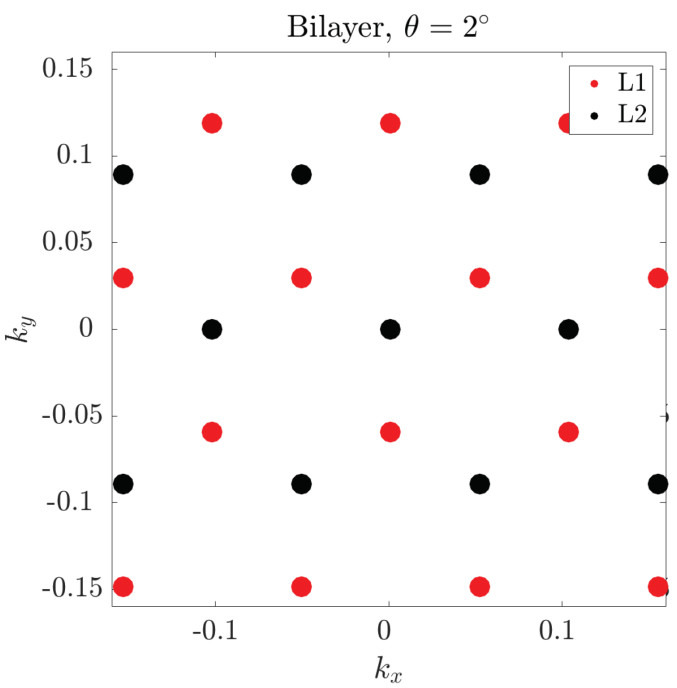

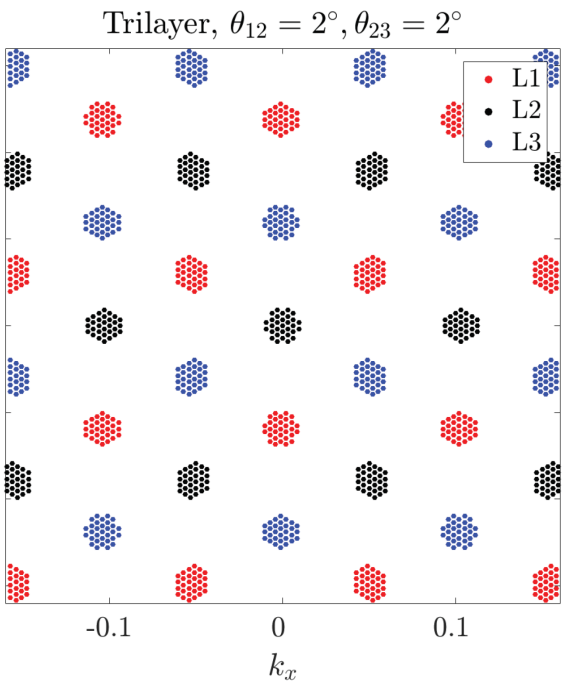

Figure: Comparison between k degrees of freedom of bilayer (left) and trilayer (right). Finite scattering between Bloch waves of the two layers in tBLG in low energy continuum approximation (Bistritzer-MacDonald model), but infinite scattering between Bloch waves of the three layers in tTLG. Convergence?

[*Twisted trilayer graphene: A precisely tunable platform for correlated electrons*, Ziyan Zhu, Stephen Carr, Daniel Massatt, Mitchell Luskin, and Efthimios Kaxiras, *Physical Review Letters*, 2020]

Band Structure Comparison Between TBLG & TTLG

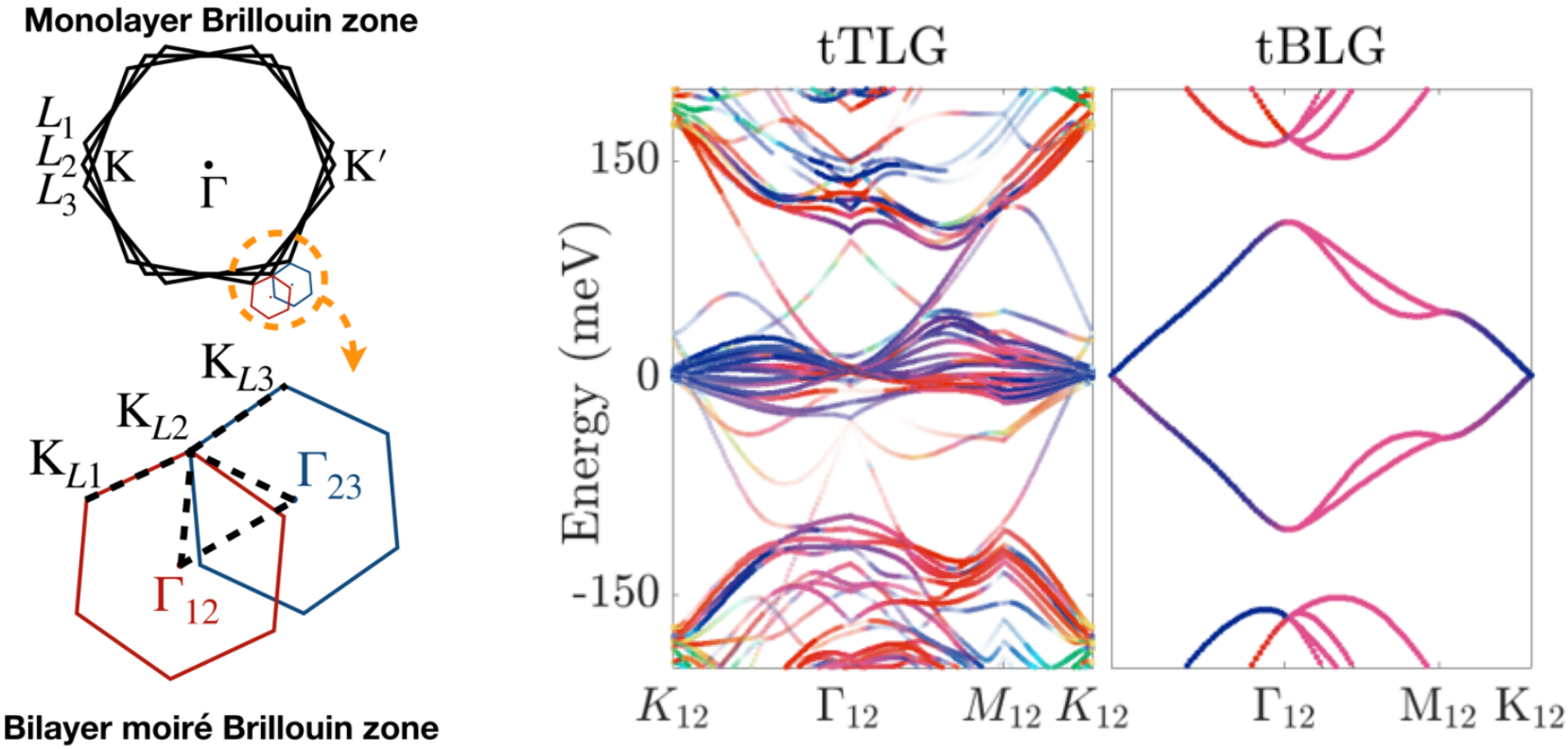

Figure: tBLG has an insolated flat band. tTTG has non-isolated and continuous bands. Band structure along the high symmetry line in the bilayer moiré Brillouin zone in tTLG $\theta_{12} = \theta_{23} = 2^\circ$ and tBLG $\theta = 2^\circ$.

[*Twisted trilayer graphene: A precisely tunable platform for correlated electrons*, Ziyan Zhu, Stephen Carr, Daniel Massatt, Mitchell Luskin, and Efthimios Kaxiras, *Physical Review Letters*, 2020]

Trilayer Superconductivity

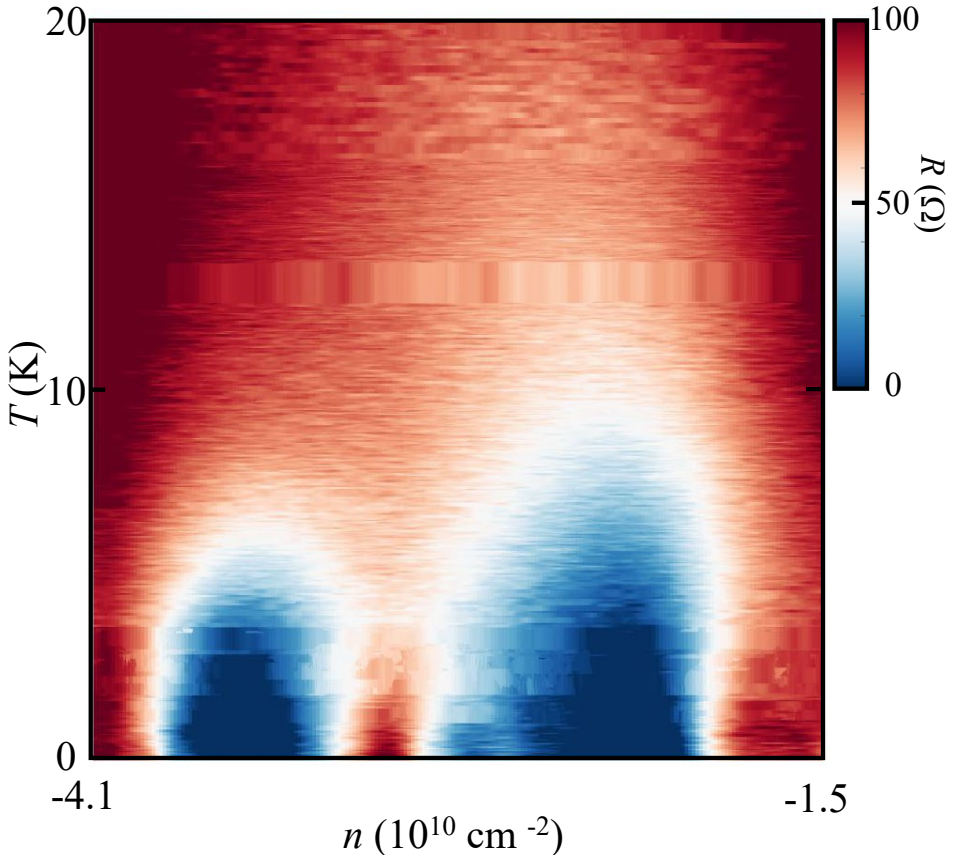

Figure: Resistance of tTLG as a function of carrier density and temperature for equal twist angles $\theta_{12} = \theta_{23} = 3.06^\circ$.
At half-filling of the moiré of moiré superlattice ($n \approx -3.2 \cdot 10^{10}\text{cm}^2$), correlated insulating behavior is observed with two adjacent superconducting domes.
Correlated insulating behavior is observed at $n \approx -1.5 \cdot 10^{12}\text{cm}^2$ in tBLG.

[*Correlated superconducting and insulating states in twisted trilayer graphene moiré of moiré superlattices,*, K-T Tsai, Xi Zhang, Ziyan Zhu, Yujie Luo, S. Carr, M. Luskin, E. Kaxiras, and Ke Wang, Phys. Rev. Lett., 2021.]

Insulating and Semimetal Behavior at Even Fillings of Moiré of Moiré Superlattices

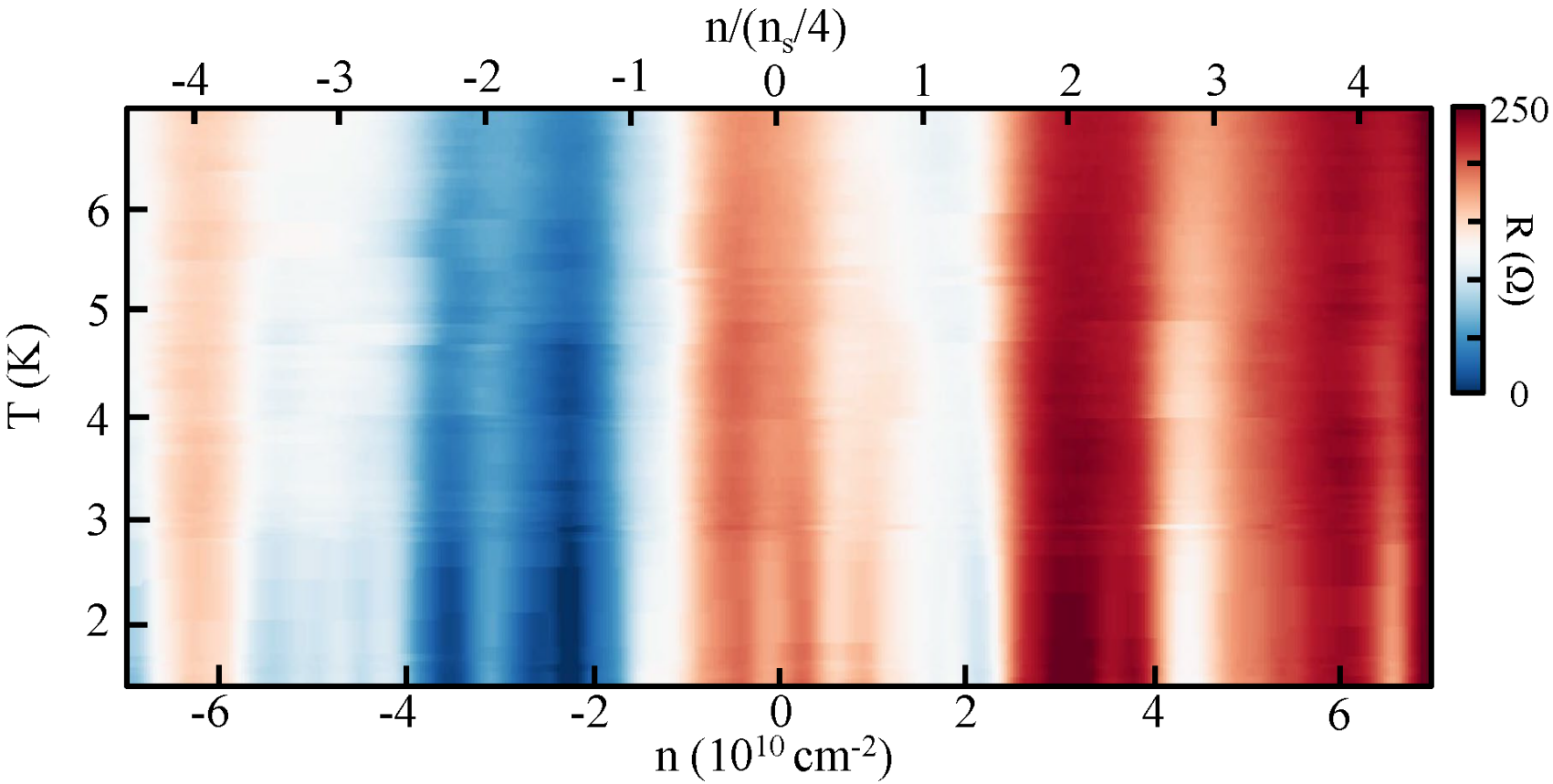

Figure: Resistance peaks are observed at all even fillings, $\nu = n/(n_s) = -4, -2, 0, 2, 4$, in which n is the carrier density and $n_s = 6.22 \cdot 10^{10}\text{cm}^2$ is the carrier density corresponding to full occupancy of the moiré of moiré unit cell.

[*Correlated superconducting and insulating states in twisted trilayer graphene moiré of moiré superlattices,*, K-T Tsai, Xi Zhang, Ziyan Zhu, Yujie Luo, S. Carr, M. Luskin, E. Kaxiras, and Ke Wang, Phys. Rev. Lett., 2021.]